Engineering Geology 352 (2025) 108054

Contents lists available at ScienceDirect

Engineering Geology

journal homepage: www.elsevier.com/locate/enggeo

A novel unified elastoplasticity-$\mu(I)$ phase transition model for granular flows from solid-like to fluid-like states and its application

Hang Feng, Zhen-Yu Yin *, Weijian Liang

Department of Civil and Environmental Engineering, The Hong Kong Polytechnic University, Hung Hom, Kowloon, Hong Kong, China

ARTICLE INFO

Keywords:
Granular soil
Constitutive model
MPM
Phase transition
Elastoplasticity
Viscosity

ABSTRACT

Accurate continuum modelling of granular flows is essential for predicting geohazards such as flow-like landslides and debris flows. Achieving such precision necessitates both a robust constitutive model for granular media and a numerical solver capable of handling large deformations. In this work, a novel unified phase transition constitutive model for granular media is proposed that follows a generalized Maxwell framework. The stress is divided into an elastoplastic part and a viscous part. The former utilizes a critical-state-based elastoplasticity model, while the latter employs a strain acceleration-based $\mu(I)$ rheology model. Key characteristics such as nonlinear elasticity, nonlinear plastic hardening, stress dilatancy, and critical state concept are incorporated into the elastoplasticity model, and the non-Newtonian $\mu(I)$ rheology model considers strain rate and strain acceleration (i.e., a higher-order derivative of strain) to capture changes in accelerated and decelerated flow conditions. A series of element tests is simulated using the proposed unified phase transition model, demonstrating that the novel theory effectively describes the transition of granular media from solid-like to fluid-like states in a unified manner. The proposed unified model is then implemented within the material point method (MPM) framework to simulate 2D and 3D granular flows. The results show remarkable consistency with results from experiments and other numerical methods, demonstrating the model's accuracy in capturing solid-like behaviour during inception and deposition, as well as liquid-like behaviour during propagation.

1. Introduction

Landslides with three stages, initiation, propagation, and deposition, are among the most hazardous geological phenomena (Li et al., 2019; Ye et al., 2024). They exhibit various movement types, such as fall, topple, and flow (Dikau and Commission, 1996). Notably, flow-like landslides, characterized by high velocity and extensive impact areas, can shape the morphography of the natural environment and induce high potential risks to man-made structures (Li et al., 2019). For example, a flow-like landslide in Valarties, Val d'Aran (Catalonia, Spain), travelled 280 m down the valley and ascended about 80 m on the opposite hillside, reshaping the geological characteristics (Di Carluccio et al., 2022). Another example is the 2001 flow-like landslide in Las Colinas (Santa Tecla, El Salvador), which caused 600 fatalities and destroyed 400 homes (Dutto, 2014). Additionally, the Yahuokou landslide in Gansu, China, with a volume of 3.92×10^6 m^3, resulted in direct economic losses exceeding 102 million CNY (Yang et al., 2024).

These flow-like landslides, closely associated with granular flows, exhibit distinct characteristics across different stages (Vescovi et al., 2013; Redaelli et al., 2016; Si et al., 2019; Berzi et al., 2022) (see Fig. 1): (i) During the initiation stage, the sliding material begins with a solid-like state in the small strain rate range, with effective stress gradually decreasing to residual strength; (ii) in the propagation stage, the sliding material demonstrates fluid-like behaviour in the large strain rate range; and (iii) in the sedimentation stage, the material ultimately deposits as solid-like substances under the frictional resistance of the terrain. Accurately modelling these complex mechanical responses of granular media, especially the intricate particle-particle interaction mechanisms during large deformation flow, is crucial for the precise analysis and prediction of geohazards, particularly flow-like landslides.

Existing literature has developed various constitutive models linking stress and deformation to describe material responses during granular flow. Soil mechanics-based models, such as elastic, elastoplastic, and hypoplastic models, effectively capture solid-like behaviour at small strain rates (e.g., Wu and Bauer, 1994; Sloan et al., 2001; Yao et al., 2009; Yin et al., 2020; Feng et al., 2024). However, they inadequately replicate post-failure behaviour at large strain rates. Conversely, fluid mechanics-based models are employed for fluid-like characteristics at

* Corresponding author.
E-mail addresses: 23039257r@connect.polyu.hk (H. Feng), zhenyu.yin@polyu.edu.hk (Z.-Y. Yin).

https://doi.org/10.1016/j.enggeo.2025.108054
Received 6 August 2024; Received in revised form 23 January 2025; Accepted 28 March 2025
Available online 4 April 2025

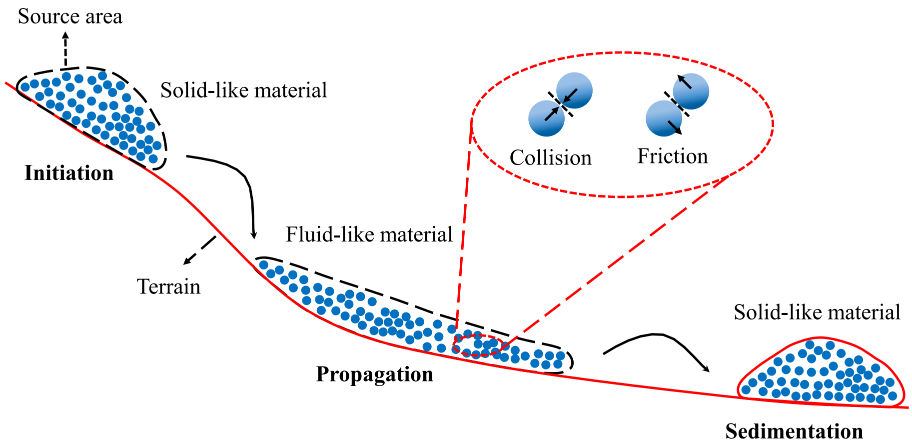

Fig. 1. The movement of granular material during the flow-like landslide.

Table 1
Existing solid-fluid phase transition models using the frictional-collisional framework.

Reference	Frictional stress					Collisional stress
	Type	Nonlinear elasticity	Nonlinear plastic hardening	Stress dilatancy	Critical state	Type
Guo et al. (2016); Peng et al. (2016); Guo et al. (2021); Wang and Wu (2024)	Hypoplastic model	×	×	√	√	Bagnold-based model; Modified $\mu(I)$ model
Vescovi et al. (2013); Redaelli et al. (2016)	Elastoplastic model	×	×	×	√	Kinetic theory
Si et al. (2019)	Elastoplastic model	×	×	×	×	Kinetic theory
Xu et al. (2019)	Elastoplastic model	×	×	×	×	$\mu(I)$ model
Marveggio et al. (2022)	Elastoplastic model	×	√	√	√	Kinetic theory
This study	**Elastoplastic model**	√	√	√	√	**Modified $\mu(I)$ model**

high strain rates (e.g., Franci and Cremonesi, 2019), yet they fail to capture solid-like responses at small deformations. Given these characteristics, neither soil mechanics-based nor fluid mechanics-based models can fully capture the initiation and propagation stages of granular flow. Therefore, it is crucial to propose a robust model that effectively addresses these issues.

Many studies have developed advanced constitutive models that depict the phase transition from solid-like to fluid-like states in granular flow, integrating interdisciplinary ideas including elasticity, plasticity, and viscosity from theories of soil mechanics and fluid dynamics. These models have the following categories based on their representations of elastic, plastic, and viscous behaviours: (i) Rate-based elasto-viscoplastic model. It consists of an elastic spring in series with a viscoplastic part (e.g., Pastor et al., 2015a, 2015b; Manzanal et al., 2016). Notably, Pastor et al. (2015a) employed Perzyna's elasto-viscoplastic models (Perzyna, 1963) to describe the solid-fluid phase transition behaviour for cohesive-viscous materials. (ii) Rate-based elastoplastic model. It includes a rate-based elastic spring and a rate-based plastic slider connected in series (e.g., Kamrin, 2010; Dunatunga and Kamrin, 2015; Baumgarten and Kamrin, 2019). In these models, the rheology relation is incorporated in the plastic flow rule to consider the rete-dependence. (iii) Hydrodynamic-plastic model (Alaei et al., 2021), which integrates the hydrodynamic idea (see Landau and Lifshitz, 1987) with the plasticity theory to describe the rate-dependent and rate-independent characteristics. (iv) Generalized Maxwell framework-based model (i.e., unified frictional-collisional framework in this study) (e.g., Vescovi et al., 2013; Guo et al., 2016; Peng et al., 2016; Si et al., 2019; Vescovi et al., 2020a; Vescovi et al., 2020b; Redaelli et al., 2016; Wu et al., 2020; Guo et al., 2021; Berzi et al., 2022; Marveggio et al., 2022; Wang and Wu, 2024). It consists of an elastic spring and a plastic slider connected in series, in parallel with a viscous dashpot. The total stress is divided into a rate-independent frictional stress (i.e., elastic spring and a plastic slider) and a rate-dependent collisional stress (i.e., viscous dashpot), each of which can be seen as representing solid-like and fluid-like stresses. This study follows the generalized Maxwell framework to establish a robust unified phase transition model for granular flows from solid-like to fluid-like states.

To the authors' knowledge, existing unified frictional-collisional models from solid-like to fluid-like states can be categorized based on their treatment of frictional stress (see Table 1): hypoplastic-based (e.g., Peng et al., 2016; Guo et al., 2021; Wang and Wu, 2024) and elastoplastic-based models (e.g., Vescovi et al., 2013; Redaelli et al., 2016; Marveggio et al., 2022); Hypoplastic-based models integrate a hypoplastic framework, developed independently of elastoplastic theory, for frictional stress, along with viscous models such as the Bagnold-based models and modified $\mu(I)$ models to describe collisional stress. These models effectively capture fluid-like responses using straightforward viscous formulations. In contrast, the elastoplastic-based model utilizes elastoplastic theory to describe frictional stress. Considering that it can effectively differentiate between elastic and plastic responses (see Table 1), we employ the elastoplasticity-based model to depict the granular flow.

In the existing literature, early efforts by Vescovi et al. (2013) and Redaelli et al. (2016) proposed elastoplastic models with critical state concepts to describe the frictional mechanism of granular flows and employed kinetic theory with a state variable, granular temperature, to model collisional mechanism. Marveggio et al. (2022) further developed a model combining strain-hardening elastoplasticity and kinetic theory, which can consider the role of isotropic softening/hardening, critical state, and stress dilatancy. The employed kinetic theory is irrelated to strain acceleration. In addition, Xu et al. (2019) developed a phase transition model utilizing the $\mu(I)$ viscosity but neglected the critical state concept. Up to now, a comprehensive and simple elastoplasticity-based phase transition model that accurately describes the following key characteristics is still under investigation: (i) the progression from the initial state to the critical state within solid-like conditions; (ii) essential features such as nonlinear elasticity, nonlinear plasticity, and the phenomena of stress-induced shear hardening or softening within solid-like conditions; and (iii) dependence on the strain acceleration in fluid-like conditions. Thus, a comprehensive constitutive model to address these issues should be proposed.

Accurate modelling of granular flows requires not only a robust constitutive model but also an effective numerical solver. Traditional Lagrangian-based methods, such as the finite element method (FEM), face significant mesh distortion challenges when addressing large deformation problems. In contrast, Eulerian-based approaches, such as the finite volume method (FVM) and finite difference method (FDM), struggle to accurately capture free surfaces of granular flow. Consequently, neither traditional Lagrangian-based nor Eulerian-based methods can fully rationally represent granular flow. Alternative particle-based methods, such as the Material Point Method (MPM) (e.g., Liu et al., 2022; Urmi et al., 2024; Shen et al., 2024), Particle Finite Element Method (PFEM) (e.g., Jin et al., 2020), and Smoothed Particle Hydrodynamics (SPH) (e.g., Su et al., 2024), effectively overcome these limitations. In this study, we have chosen the MPM as our numerical solver for this study.

Motivated by the above considerations, this study aims to develop a novel unified elastoplasticity-$\mu(I)$ phase transition constitutive model that completely represents the aforementioned essential characteristics in both solid-like and fluid-like phases and to implement this model into the MPM framework to model granular flow. Based on the generalized Maxwell framework, the unified phase transition model is proposed by combining a critical-state-based elastoplasticity model with a strain acceleration-based $\mu(I)$ rheology model. The critical-state-based elastoplasticity model incorporates nonlinear elasticity, nonlinear plastic hardening, stress dilatancy, and the critical state. Concurrently, the non-Newtonian $\mu(I)$ model accounts for dependences on strain rate, strain acceleration, and void ratio. To validate the effectiveness of the proposed elastoplasticity-$\mu(I)$ phase transition model, various element test simulations are conducted. Additionally, the new unified elastoplasticity-$\mu(I)$ model is incorporated into the material point method (MPM) to simulate granular flows. Both 2D and 3D granular flow simulations are performed using the MPM framework with the unified elastoplasticity-$\mu(I)$ model, thereby evaluating its effectiveness.

The paper is organized as follows: Section 2 details the proposed unified elastoplasticity-$\mu(I)$ model, while Section 3 discusses the verification of the proposed unified elastoplasticity-$\mu(I)$ model. Section 4 presents 2D and 3D numerical simulations to validate the MPM scheme with the proposed unified elastoplasticity-$\mu(I)$ model. Finally, Section 5 draws some major conclusions for the study.

2. Proposed unified elastoplasticity-$\mu(I)$ phase transition model

This section commences with a brief introduction of the generalized Maxwell framework; and then proceeds to describe the frictional stress and collisional stress part. The summary of the proposed unified elastoplasticity-$\mu(I)$ model and the model validation are then discussed.

2.1. Generalized maxwell framework

When the granular soil undergoes large deformation flows, two main particle interaction mechanisms exist: frictional and collisional. The frictional mechanism represents enduring contacts among particles, while the collisional mechanism describes particle collisions (see Fig. 1).

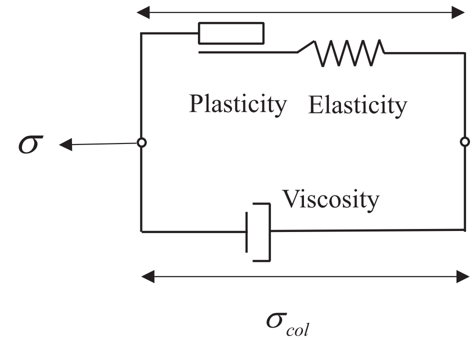

Fig. 2. Illustration of the generalized Maxwell framework for the solid-fliud phase transition model.

Frictional and collisional stress are the two mechanisms that match up (Vescovi et al., 2013; Redaelli et al., 2016; Wang and Wu, 2024). Based on these two mechanisms, granular flow can be divided into three regimes: (i) "quasi-static" regime: dominated by the friction mechanism, where the material is dense and behaves like solids in the small strain rate range. The stress is primarily frictional, also referred to as quasi-static stress. (ii) "Collisional" regime: dominated by the collision mechanism, where the granular material is loose and controlled by collisional stress in the large strain rate range. (iii) "Transitional" regime: characterized by interactions through both collision and friction, where the material behaves like fluids under the combined influence of collision-induced and friction-induced stress (Redaelli et al., 2016; Vescovi et al., 2020a, 2020b; Marveggio et al., 2022).

As shown in Fig. 2, a generalized Maxwell model is used to establish a constitutive relationship capable of addressing the aforementioned concerns. This model consists of a spring, slider, and dashpot. The upper part, a combination of a spring in series with a slider, is parallel to the lower part, which only includes a dashpot. The spring and slider represent elasticity and plasticity, respectively, while the dashpot denotes viscosity.

Within the generalized Maxwell framework, the total stress is decomposed into frictional stress from the upper part and collisional stress from the lower part (see Eq. (1)). The frictional stress $\boldsymbol{\sigma}_f$ is strain rate-independent and is described by elastoplasticity theory, while the collisional stress $\boldsymbol{\sigma}_{col}$ is strain rate-dependent and is represented by rheology model. Due to their parallel arrangement, frictional and collisional stresses coexist during granular flow. The following conditions are required to describe the phase transition from a solid-like to a fluid-like state using Eq. (1): (i) In the solid-like state, the frictional stress should effectively characterize the granular material's frictional properties, such as nonlinearity, dilatancy, and frictional yielding, while the collisional stress should be negligibly small. (ii) In the fluid-like state, the frictional stress should be minimal, while the collisional stress should accurately represent the granular flow's viscous properties.

$$\boldsymbol{\sigma} = \boldsymbol{\sigma}_f + \boldsymbol{\sigma}_{col} \tag{1}$$

where $\boldsymbol{\sigma}$ is the total Cauchy stress tensor; $\boldsymbol{\sigma}_f$ is the elastoplastic stress; $\boldsymbol{\sigma}_{col}$ is the collisional stress.

2.2. Frictional stress part

The frictional stress contribution in the small strain range has been extensively characterized by models in soil mechanics, such as the Mohr-Coulomb, von Mises, Drucker-Prager, and Cam-Clay models (Ponthot, 2002; Yao et al., 2009; Yin et al., 2020; Cheng et al., 2023; Cheng and Yin, 2024; Feng et al., 2025). These models effectively capture the fundamental frictional characteristics. Furthermore, during the initiation of granular flow (i.e., the transition from a solid-like to a fluid-like state), the granular material begins to deform indefinitely without significant changes in stresses and volume. This state can be accurately described by critical state theory (Roscoe et al., 1958; Schofield and Wroth, 1968). Therefore, utilizing a critical state-based elastoplasticity model is more effective in describing frictional stress in the phase transition model. Subsequently, numerical simulations of element tests using the frictional stress model are conducted to evaluate its performance.

2.2.1. Critical-state-based elastoplasticity model

This work employs the framework of the critical state-based sand model SIMSAND (Yin et al., 2013, 2014, 2020) to depict the frictional stress. Following the framework, the strain increment $\delta\boldsymbol{\varepsilon}$ is decomposed into an elastic increment $\delta\boldsymbol{\varepsilon}^e$ and a plastic increment $\delta\boldsymbol{\varepsilon}^p$ (see Eq. (2)). The nonlinear elasticity characteristic is considered in the elastic part. The nonlinear plastic hardening, stress dilatancy (contraction or dilation), and critical-state concept are considered in the plastic part.

$$\delta\boldsymbol{\varepsilon} = \delta\boldsymbol{\varepsilon}^e + \delta\boldsymbol{\varepsilon}^p \tag{2}$$

In the elastic part, the stress increment can be determined using the elastic strain increment as shown in Eq. (3). Herein $\mathbf{K_f}$ represents the fourth-order stiffness tensor, which depends on the elastic modulus E_f and Poisson's ratio ν. The elastic modulus E_f is defined by Eq. (4) to incorporate dependencies on the void ratio and hydrostatic component of frictional stress.

$$\delta\boldsymbol{\sigma}_f = \mathbf{K}_f : \delta\boldsymbol{\varepsilon}^e \tag{3}$$

$$E_f = E_0 p_{at}\frac{(2.97-e)^2}{(1+e)}\left(\frac{p_f}{p_{at}}\right)^n \tag{4}$$

where p_{at} is atmospheric pressure (i.e., $p_{at} = 101.3$ kPa); n is the elastic constant controlling nonlinear stiffness; p_f is the hydrostatic part of frictional stress; e is the void ratio.

The plastic behaviour can be determined by the yield criterion, hardening rule, and flow rule, as follows:

1. Frictional yield criterion:

The well-known Mohr-Coulomb yield criterion is employed, which is expressed as:

$$f_f = \frac{q_f}{p_f} - H_f \tag{5}$$

where q_f is the deviatoric part of frictional stress; H_f is the hardening parameter.

2. Nonlinear plastic hardening rule:

A hardening rule in hyperbolic form is employed, as follows:

$$H_f = \frac{M_p \varepsilon_d^p}{k_p + \varepsilon_d^p} \tag{6}$$

where M_p is the slope of the failure line in the p_f-q_f plane, which is expressed as $M_p = 6\sin\phi_c/(3-\sin\phi_c)$ (where ϕ_c is the friction angle) in triaxial compression condition (Lode angle effect is introduced to follow the Mohr-Coulomb criterion). ε_d^p is the plastic deviatoric strain. k_p is a constant controlling the plastic hardening behaviour.

3. Flow rule with stress dilatancy characteristic:

To consider the stress dilatancy (contraction or dilation), a parameter A_d is often introduced in plastic potential function g, as proposed by Nova and Wood (1982), Jefferies (1993), Gajo and Wood (1999), Li et al. (1999), Yang and Muraleetharan (2003), which can be expressed as follows:

Table 2
Input parameters in the frictional stress part.

Parameters	Definition	Analysis	Wichtmann (2016)
E_0	Dimensionless referential elastic modulus	150.00	50.00
ν	Poisson's ratio	0.20	0.15
n	Constant controlling nonlinear elastic stiffness	0.60	0.60
φ_c	Critical-state friction angle	23.00	31.3
e_{ref}	Initial critical-state void ratio	0.907	1.05
Λ	Constant controlling CSL nonlinearity	0.022	0.0579
ξ	Constant controlling CSL nonlinearity	0.71	0.4
A_d	Constant controlling stress dilatancy magnitude	0.50	2
k_p	Plastic modulus-related constant	0.001	0.01
n_p	Peak strength parameter	1.00	2.4
n_d	Phase transformation parameter	1.00	2.9

$$\frac{\partial g}{\partial p_f} = A_d\left(M_{pt} - \frac{q_f}{p_f}\right), \frac{\partial g}{\partial q_f} = 1 \tag{7}$$

where A_d is a parameter controlling the magnitude of the stress-dilatancy; M_{pt} is the transformation stress ratio corresponding to the transitional state between a contractive and a dilatant behaviour. If the current stress ratio is smaller than M_{pt}, the material is contractive. Otherwise, it is dilative.

4. Critical state concept:

The critical void ratio e_c is considered:

$$e_c = e_{\mathrm{ref}}\exp\left[-\Lambda\left(\frac{p_f}{p_{at}}\right)^\xi\right] \tag{8}$$

where e_{ref} is the initial critical-state void ratio; Λ is the slope of the critical state line (CSL) in the e-log p_f plane; parameter ξ controls the nonlinearity of the critical state line.

The critical-state theory is implemented in the SIMSAND model by modifying the peak stress ratio M_p and phase transformation stress ratio M_{pt} via $M_p = 6\sin\phi_p/\left(3-\sin\phi_p\right)$ and $M_{pt} = 6\sin\phi_{pt}/\left(3-\sin\phi_{pt}\right)$, respectively. The peak friction angle ϕ_p and transformation angle ϕ_{pt} are expressed as:

$$\phi_p = \arctan\left[\left(\frac{e_c}{e}\right)^{n_p}\tan\phi_c\right] \tag{9}$$

$$\phi_{pt} = \arctan\left[\left(\frac{e}{e_c}\right)^{n_d}\tan\phi_c\right] \tag{10}$$

where n_p and n_d are parameters controlling the effect of particle interlocking. When the granular material is dense (i.e., $e < e_c$), ϕ_{pt} is initially smaller than ϕ_c, representing a dense structure that is initially contractive and then dilative. When the material is loose (i.e., $e > e_c$), ϕ_{pt} is larger than ϕ_c, which leads to contractive behaviour. Both loose and dense materials will arrive at the critical state, resulting in the phase transition in the granular flow.

In summary, Eqs. (2)~(10) describe the frictional stress contribution using a critical-state-based elastoplastic model. The nonlinear elasticity, dilatancy (contraction or dilation), nonlinear plastic hardening, and critical state concept are well considered in the solid-like state of granular material. The parameters required are listed in Table 2.

2.2.2. Element test simulation

The undrained simple shear test is the available element test capable

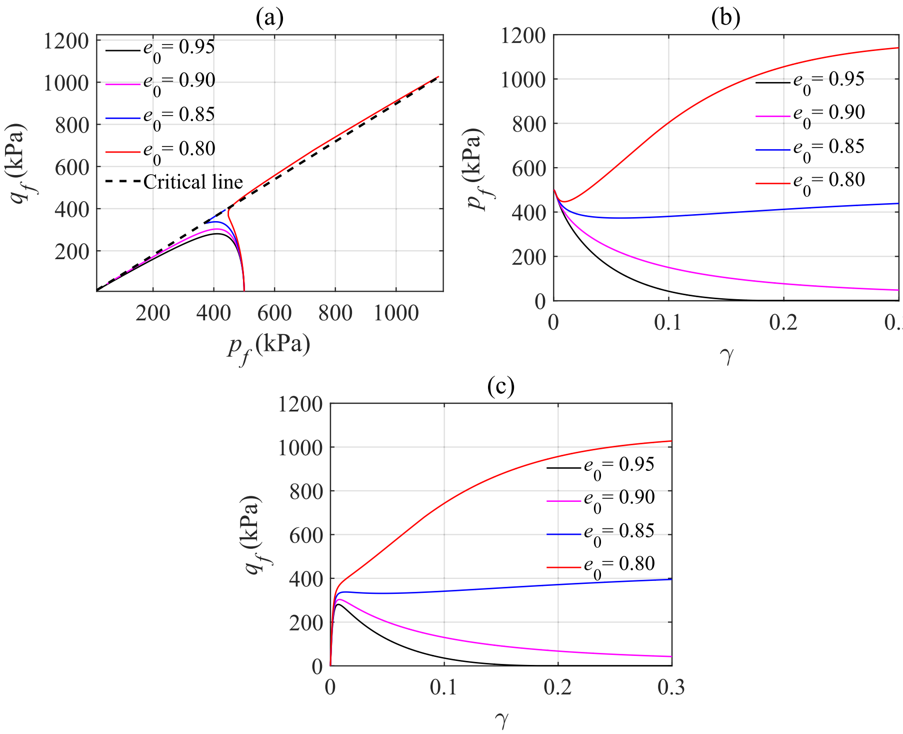

Fig. 3. Simulation results of the undrained simple shear test using the critical-state-based sand model with different initial void ratios: (a) relation between the hydrostatic stress and deviatoric stress; (b) relation between the deviatoric strain and hydrostatic stress; (c) relation between the deviatoric strain and deviatoric stress.

of exhibiting large deformation characteristics, demonstrating solid-like behaviour at low strain rates and fluid-like behaviour at high strain rates. Additionally, it can reveal the liquefaction phenomenon and has been widely employed to investigate the phase transition model (e.g., Guo et al., 2016; Peng et al., 2016; Guo et al., 2021; Wang and Wu, 2024). Hence the undrained simple shear tests are employed in this work. The details of undrained simple shear tests are listed in Appendix A. This section investigates the proposed model's performance in describing the phase transition through the numerical integration of undrained simple shear tests. Herein, a forward Eulerian explicit

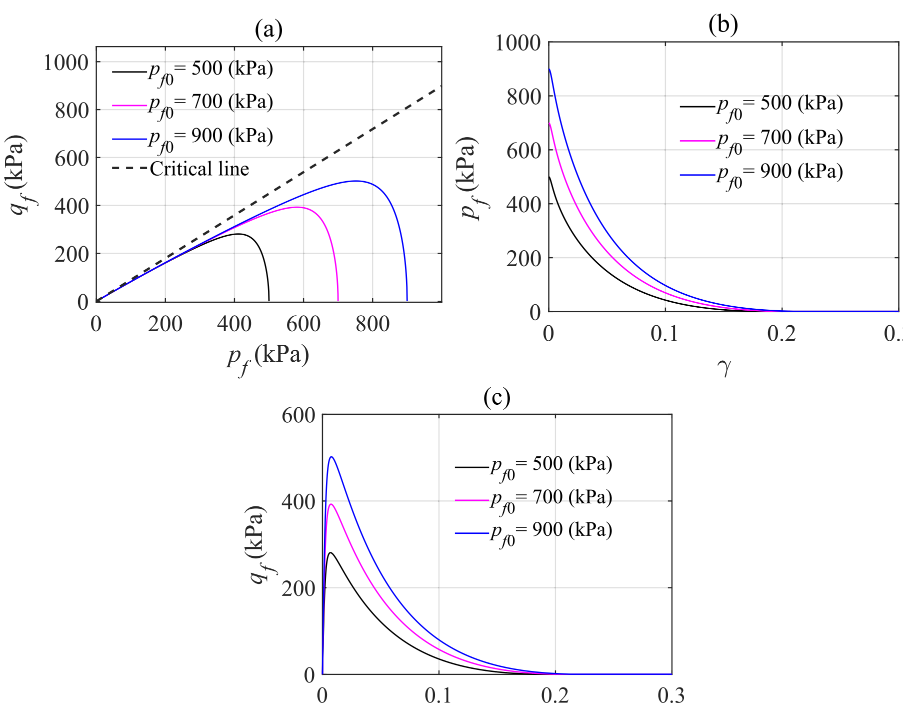

Fig. 4. Simulation results of the undrained simple shear test with different initial vertical stress: (a) relation between the hydrostatic stress and deviatoric stress; (b) relation between the deviatoric strain and hydrostatic stress; (c) relation between the deviatoric strain and deviatoric stress.

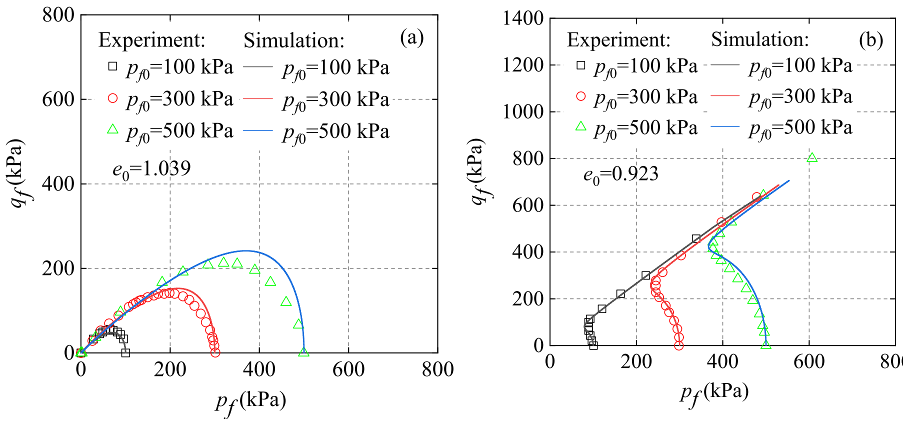

Fig. 5. Comparison of the undrained triaxial test from simulation solution and experimental results by Wichtmann (2016): (a) loose sample: $e_0 = 1.039$; (b) dense sample: $e_0 = 0.923$.

integration algorithm is employed (see Eq. (11)). Considering the strain rate-independent characteristic, only the shear strain is given, which is 0.3. A small time step $dt = 10^{-6}$ s is employed to guarantee the numerical convergence. The input parameters are listed in Table 2. Two groups of numerical integration are employed to investigate the influence of initial void ratio and initial pressure: i). The initial pressure p_{f0} is set at 500 kPa with different initial void ratios $e_0 = 0.95$, 0.90, 0.85, and 0.80; and ii) The initial void ratio e_0 is set at 0.95 with different initial pressures $p_{f0} = 500$, 700, and 900 kPa. It is worth noting that p_f and q_f are employed to denote the effective hydrostatic stress and effective deviatoric stress in the undrained test, respectively. γ is used to denote the shear strain.

$$\boldsymbol{\sigma}_f^{t+1} = \boldsymbol{\sigma}_f^t + \delta\boldsymbol{\sigma}_f = \boldsymbol{\sigma}_f^t + \mathbf{K}^t : (\delta\boldsymbol{\varepsilon} - \delta\boldsymbol{\varepsilon}^p) \tag{11}$$

Fig. 3 shows the simulation results of the undrained simple shear tests with different initial void ratios. Fig. 3(a) demonstrates that all the specimens reach the critical-state line, triggering the initiation of granular flow (i.e., the transition from a solid-like to a fluid-like state). Fig. 3 (b) and (c) show that the dense specimen (i.e., $e_0 = 0.80$) exhibits shear-hardening and dilation characteristics. The very loose specimens (i.e., $e_0 = 0.95$, 0.90) behave with the shear-softening characteristic and reach complete liquefaction, resulting in residual stress. The specimen with a medium void ratio (i.e., $e_0 = 0.85$) first behaves with the shear-softening characteristic and then with the shear-hardening characteristic. Notably, the proposed critical-state-based elastoplastic sand model performs similarly to the hypoplastic model of Wu et al. (2020), both effectively describing the dependence on the void ratio.

To further investigate the proposed critical-state-based elastoplastic sand model, the specimens with different initial vertical stress p_{f0} of 500, 700, and 900 kPa are employed. As is shown in Fig. 4, specimens with different vertical stresses arrive at the critical-state line. All the specimens behave with the shear-softening behaviour and obtain complete liquefaction, which indicates the established frictional stress model can effectively describe the mechanism in the liquefaction of debris flows and can be rational in depicting the initiation of granular flow.

To validate the critical-state-based sand model, the experimental results from Wichtmann (2016) are utilized and presented herein. In the prototype experiment, three different initial pressures p_{f0} of 100, 300, and 500 kPa were applied. To obtain the parameters for the proposed frictional stress model, the calibration process outlined in Appendix C is followed. First, the critical-state line (CSL) reported by Wichtmann (2016) is used to determine the values of e_{ref}, Λ, and ξ, with fitted values of 1.05, 0.0579, and 0.4, respectively. The second determination involves the elastic parameters. Poisson's ratio ν is set to a typical value of 0.15, while the elastic modulus coefficient E_0 and n are assigned values of 50 and 0.6, respectively, to reflect the small stiffness reported by Wichtmann (2016). The friction angle φ_c is reported as 23°, and two different initial void ratios, 1.039 and 0.923, are obtained using the initial relative density. Finally, the parameters A_d and k_p are assigned typical values of 2 and 0.01, n_p and n_d are set as 2.4 and 2.9 based on the values reported for Toyoura Sand (see Yin et al., 2018).

Fig. 5 compares the simulation results using the critical-state-based frictional stress model with the experimental results from Wichtmann (2016). Both the simulation and experiment stresses with different initial void ratios, travel along the critical-state line (CSL), showing good agreement. This demonstrates the effectiveness of the critical-state-based frictional stress model.

2.3. Collisional stress part

When granular material is fluid-like, it is mainly controlled by collisional stress, which can be depicted using a viscous stress model (e.g., Jop et al., 2006; Vescovi et al., 2013; Redaelli et al., 2016). Most of these models are based on the relationship between stress and strain rate and cannot consider different viscous behaviours under acceleration and deceleration. Hence, a higher-order derivative of strain is more rational for considering the acceleration effect of granular flow in the large strain range stage. This section uses a strain acceleration-based non-Newtonian $\mu(I)$ model to depict the collisional stress in the Generalized Maxwell model. Numerical simulations of element tests are then performed to investigate this model's effectiveness.

2.3.1. Stain acceleration-based $\mu(I)$ model

In this work, the framework of collisional stress proposed by Wang and Wu (2024) is employed to depict the collisional stress contribution in the generalized Maxwell model. Following the framework, the collisional stress is expressed in rate form, which is expressed as follows:

$$\dot{\boldsymbol{\sigma}}_{col} = f_\Phi(2\mu|\dot{\gamma}|\ddot{\mathbf{e}} - \dot{\mathbf{e}}\ddot{\mathbf{e}} - \ddot{\mathbf{e}}\dot{\mathbf{e}}) \tag{12}$$

where $\dot{\mathbf{e}}$ is the deviatoric part of the strain rate tensor, defined as $\dot{\mathbf{e}} = \dot{\boldsymbol{\varepsilon}} - \text{tr}(\dot{\boldsymbol{\varepsilon}})\mathbf{I}/3$ (in which $\dot{\boldsymbol{\varepsilon}}$ is the first time-derivation of the strain tensor expressed in Eq. (13)); $\ddot{\mathbf{e}}$ is the deviatoric part of the strain acceleration tensor, defined as $\ddot{\mathbf{e}} = \ddot{\boldsymbol{\varepsilon}} - \text{tr}(\ddot{\boldsymbol{\varepsilon}})\mathbf{I}/3$ (in which $\ddot{\boldsymbol{\varepsilon}}$ is the second time-derivation of the strain tensor expressed in Eq.(14)); $|\dot{\gamma}|$ is the second invariant of the deviatoric strain rate tensor, expressed as $|\dot{\gamma}| = \sqrt{\dot{\mathbf{e}} : \dot{\mathbf{e}}/2}$. μ is a friction coefficient. f_Φ is the function of the volume fraction of the granular material Φ, effectively describing the dependence on the void ratio.

The first time-derivation of the strain tensor (i.e., strain rate tensor) and second time-derivation of the strain tensor (i.e., strain acceleration tensor) are expressed as follows:

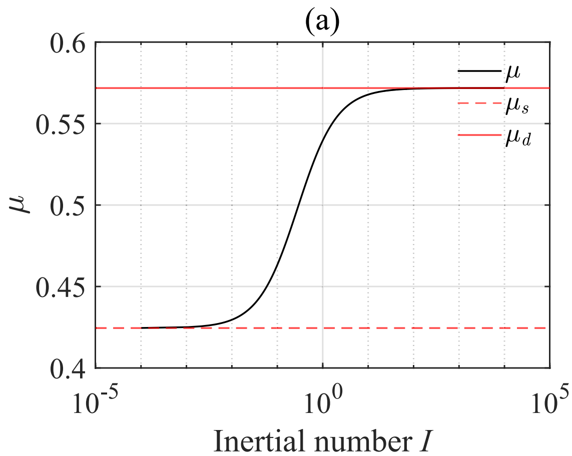

Fig. 6. Relation between the friction coefficient μ and the inertial number I (μ_s=0.4245; μ_d=0.5718; $d = 10^{-3}$ m; ρ_s=1090 kg/m^3, $I_0 = 0.28$).

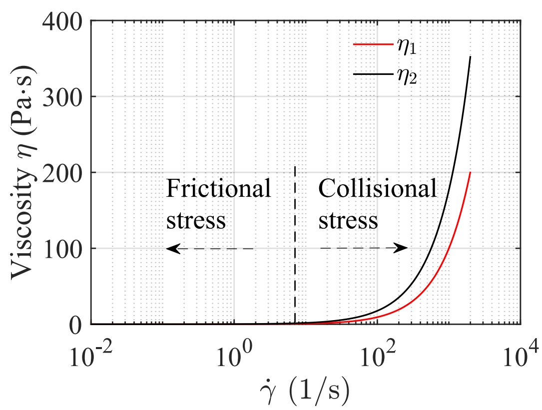

Fig. 7. Relation between the viscosity η and shear rate $\dot{\gamma}$ ($\mu_s = 0.4245$; $\mu_d = 0.5718$;$d = 10^{-3}$ m; ρ_s=1090 kg/m^3, $I_0 = 0.28$, $\Delta\Phi$=0.29, Φ_c=0.62).

$$\dot{\boldsymbol{\varepsilon}} = \frac{1}{2}\left(\nabla\mathbf{v} + \nabla\mathbf{v}^T\right) \tag{13}$$

$$\ddot{\boldsymbol{\varepsilon}} = \frac{1}{2}\left(\nabla\dot{\mathbf{v}} + \nabla\dot{\mathbf{v}}^T\right) \tag{14}$$

where $\mathbf{v}$ is the velocity tensor; $\nabla\mathbf{v}$ represents the velocity gradient.

The function of the volume fraction f_Φ, expressed as follows:

$$f_\Phi = \rho_s\left(2d\frac{\Delta\Phi}{\Phi_c - \Phi}\right)^2 \tag{15}$$

where Φ is the volume fraction of the granular material, related to the void ratio via $1/(1+e)$; ρ_s denotes the density of the granular particle; d is the diameter of the particle; Φ_c represents the random close packing volume fraction; $\Delta\Phi$ is the dynamic loosening coefficient.

In the fluid-like state, the friction coefficient μ is significant to depict the relation between the shear part and the hydrostatic part. Jop et al. (2006) established the $\mu(I)$ model to describe the rheology of the granular matter, which is expressed as follows:

$$\mu(I) = \mu_s + \frac{\mu_d - \mu_s}{I_0 + I}I \tag{16}$$

where inertial number I represents the ratio between the time scales of deformation and the structural confinement of particles, defined as $I = 2d|\dot{\gamma}|/\sqrt{p/\rho_s}$ (Note p is the hydrostatic part of the total stress in the generalized Maxwell model). I_0 is a referential inertial number; μ_s and μ_d are the static and dynamic friction coefficient, respectively (Note that μ_s can be related to friction angle ϕ_c in a solid-like state via $\mu_s = \tan\phi_c$). An example of the $\mu(I)$ model is expressed in Fig. 6. which indicates that the friction coefficient tends to be μ_s for the minimal inertial number while it tends to be μ_d for the large inertial number.

Table 3
Input parameters in the collisional stress part.

Parameters	Definitions	Values
I_0	Referential inertial ratio	0.28
Φ_c	Random close volume fraction	0.62
$\Delta\Phi$	Dynamic loosening factor	0.29
ρ_s	Particle density (kg/m^3)	1090.00
μ_s	Static friction coefficient ($\tan\varphi_c$)	0.4245
μ_d	Dynamic friction coefficient	0.5718
d	Particle diameter (m)	1.0×10^{-3}

In the strain acceleration-based non-Newtonian $\mu(I)$ model, the equivalent shear viscosity coefficient can be expressed as $\eta_1 = 2\mu|\dot{\gamma}|f_\Phi$ while an equivalent bulk viscosity coefficient can be described via $\eta_2 = 2|\dot{\gamma}|f_\Phi$. Fig. 7 shows a typical example of these equivalent viscosity coefficients. The viscosity coefficients are negligible in the small strain rate regime while are significant for the large strain rate regime, indicating the strain acceleration-based non-Newtonian $\mu(I)$ model effectively satisfies the requirement of the phase transition model: i). The collisional stress $\boldsymbol{\sigma}_{col}$ should be negligibly small in the solid-like state ii). The material is controlled by the collisional stress when the material is in a fluid-like state.

2.3.2. Element test simulation

This section investigates the collisional stress model's performance via the numerical integration of undrained simple shear tests. Details of the collisional stress in the undrained simple shear tests are listed in Appendix B. As is shown in Eq. (17), a forward Eulerian explicit integration algorithm is employed. A small-time step $dt = 10^{-6}$ s is employed. The model parameters from Franci and Cremonesi (2019) and Wang and Wu (2024) listed in Table 3, are adopted.

$$\boldsymbol{\sigma}_{col}^{t+1} = \boldsymbol{\sigma}_{col}^{t} + \dot{\boldsymbol{\sigma}}_{col}^{t}dt \tag{17}$$

To investigate the capability of the established non-Newtonian $\mu(I)$ model in describing the strain rate-dependent, strain acceleration-dependent, and void ratio-dependent characteristics, two groups of numerical integration are employed: i). Three different strain rate paths depicting the time evolution of strain rate and acceleration are adopted, shown in Fig. 8, with an initial void ratio $e_0 = 0.80$. ii) Different void ratios of 0.80, 0.85, 0.90, and 0.95 are employed with strain rate path 1 in Fig. 8. Two groups adopt the same initial pressure of 100 kPa. It is worth noting that p_{col} and q_{col} are employed to denote the effective vertical stress and effective shear stress of the collisional stress contribution, respectively. γ denotes the shear strain, while $\dot{\gamma}$ and $\ddot{\gamma}$ represent the shear rate and acceleration, respectively.

Fig. 9 shows the simulation results of the undrained simple shear test using the strain acceleration-based non-Newtonian $\mu(I)$ model. In path 1, the strain acceleration changes from a positive to a zero, then to a negative value. The strain rate first increases, then keeps constant, followed by a decrease. The hydrostatic stress p_{col} and deviatoric stress q_{col} under this strain rate path first increase, then remain constant, and then decrease, which matches well with the evolution of $\dot{\gamma}\ddot{\gamma}$. In path 2, the strain acceleration of the granular material varies from a positive to a negative, then to a positive value. The strain rate experiences an increase, followed by a decrease, and then a rise. The hydrostatic stress p_{col} and deviatoric stress q_{col} under strain rate path 2 have the same tendency as $\dot{\gamma}\ddot{\gamma}$. In path 3, there is a constant strain acceleration and an increasing strain rate. The corresponding collisional stress gradually increases. These results under different strain rate paths demonstrate that the non-Newtonian $\mu(I)$ model effectively describes the strain rate-dependent

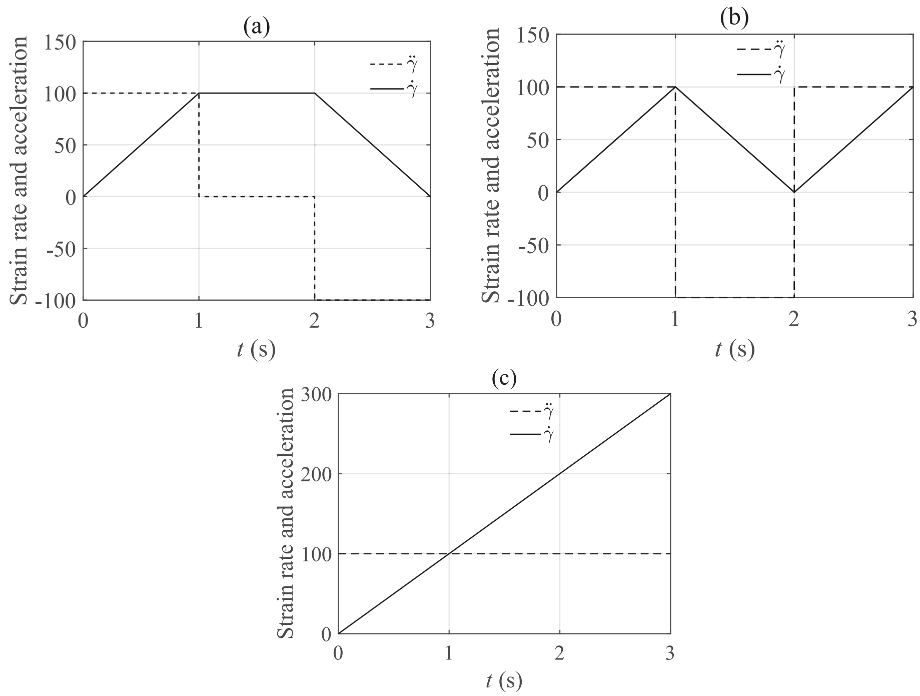

Fig. 8. Different strain rate paths depicting the evolution of strain rate and acceleration: (a) Path 1 (Variable strain acceleration); (b) Path 2 (Variable strain acceleration); (c) Path 3 (Constant strain acceleration).

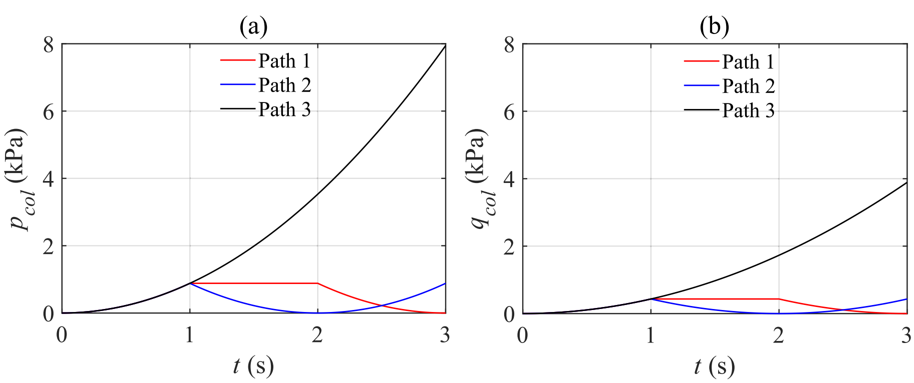

Fig. 9. Simulation results using the strain acceleration-based non-Newtonian $\mu(I)$ model with different strain paths ($e_0 = 0.80$, $p_0 = 100$ kPa) (a) relation between the hydrostatic stress and time; (b) relation between the deviatoric stress and time.

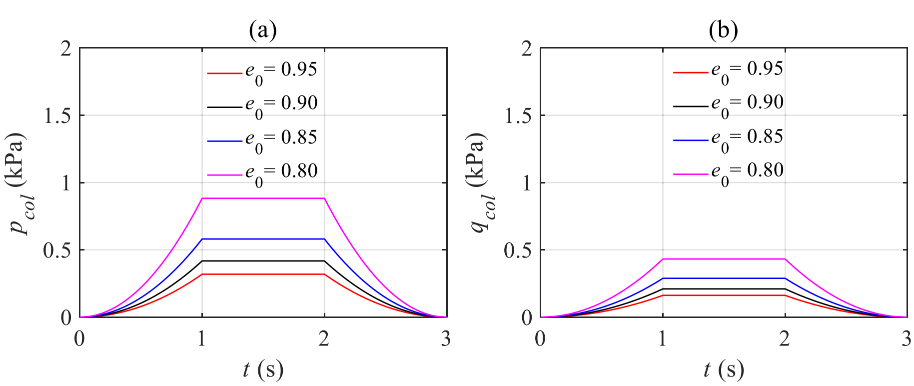

Fig. 10. Simulation results using the strain acceleration-based non-Newtonian $\mu(I)$ model with different initial void ratios (Strain path 1, $p_0 = 100$ kPa) (a) relation between the hydrostatic stress and time; (b) relation between the deviatoric stress and time.

Table 4
Basic input parameters in the proposed unified elastoplasticity-$\mu(I)$ model.

Stress type	Parameter	Definition	Reference value				
			Polystyrene	Glass	DEM data	MPM Case 1	MPM Case 2
Elastoplastic stress	E_0	Dimensionless referential elastic modulus	190.00	200.00	200.00	150.00	100.00
	ν	Poisson's ratio	0.235	0.235	0.235	0.2	0.2
	n	Constant controlling nonlinear elastic stiffness	0.60	0.60	0.60	0.50	0.50
	φ_c	Critical-state friction angle	23.00	25.00	21.11	18.9	16.7
	e_0	Initial void ratio	–	–	–	0.85	0.85
	e_{ref}	Initial critical-state void ratio	0.910	0.917	0.750	0.877	0.977
	Λ	Constant controlling CSL nonlinearity	0.122	0.122	0.122	0.0596	0.0596
	ξ	Constant controlling CSL nonlinearity	0.71	0.71	0.71	0.365	0.365
	A_d	Constant controlling stress dilatancy magnitude	0.5	0.5	0.5	0.7	0.7
	k_p	Plastic modulus–related constant	0.001	0.001	0.001	0.0044	0.0044
	n_p	Peak strength parameter	1	1	1	2.4	2.4
	n_d	Phase transformation parameter	1	1	1	2.9	2.9
Viscous stress	I_0	Referential inertial ratio	0.28	0.28	0.48	0.28	0.20
	ρ_s	Particle density (kg/m^3)	1050.00	2970.00	1000.00	2500.00	2500.00
	d	Particle diameter (m)	$1.0{\cdot}10^{-3}$	$1.8{\cdot}10^{-3}$	$2{\cdot}10^{-5}$	$1.0{\cdot}10^{-3}$	$1.0{\cdot}10^{-3}$
	μ_s	Static friction coefficient (tanφ)	0.4245	0.4660	0.386	0.38	0.30
	μ_d	Dynamic friction coefficient	0.5774	0.5774	0.610	0.66	0.70
	Φ_c	Random close volume fraction	0.62	0.62	0.64	0.70	0.70
	$\Delta\Phi$	Dynamic loosening factor	0.29	0.22	0.18	0.29	0.20

and strain acceleration-dependent characteristics. It is also observed that the hydrostatic stress p_{col} and deviatoric stress q_{col} have the same evolution tendency but different values, indicating this model effectively expresses the effect of friction coefficient μ.

Fig. 10 shows the simulation results of the undrained simple shear test using the collisional stress model under different initial void ratios. The results indicate that the loose specimens have smaller collisional stress than the dense specimens, matching the dependence of the frictional stress on the void ratio in subsection 2.2. This indicates the established non-Newtonian $\mu(I)$ model can effectively describe the void ratio-dependent characteristics.

2.4. Unified elasticity-$\mu(I)$ phase transition model

2.4.1. Unified model

Following the generalized Maxwell framework, the unified phase transition model is proposed by combining both frictional and collisional contributions. Using the explicit form, the unified stress is expressed as follows:

$$\boldsymbol{\sigma}^{t+1} = \boldsymbol{\sigma}_{col}^{t+1} + \boldsymbol{\sigma}_f^{t+1} = \boldsymbol{\sigma}_{col}^{t} + \boldsymbol{\sigma}_f^{t} + \dot{\boldsymbol{\sigma}}_{col}^{t} dt + \mathbf{K}^t : (\delta\boldsymbol{\varepsilon}^t - \delta\boldsymbol{\varepsilon}^{t,p}) \tag{18}$$

This proposed phase transition model employs the strain rate-independent stress in the critical-state-based elastoplastic model to depict the frictional interaction, while using strain rate-dependent and strain acceleration-dependent stress in Non-Newtonian $\mu(I)$ model to describe the collisional interaction. From the solid-like to fluid-like state, the dominant stress controlling the granular behaviour changes from frictional to collisional stress. This model can not only reproduce the solid-like behaviours, such as nonlinear elasticity, nonlinear plastic hardening, stress dilatancy (contraction or dilation), and critical state characteristics but also capture the non-Newtonian fluid-like behaviours. Note that this study assumes that frictional stress is rate-independent, i.e., the critical state line (CSL) does not vary with strain rate. The rate-induced dilatancy described by Bagnold (1954) is only considered for collisional stress. Future work should propose a modified phase transition model that incorporates rate-dependent characteristics, specifically a dynamical critical state line, as suggested by Pastor et al. (2015c).

The basic input parameters in this unified phase transition model are summarized in Table 4. Important input parameters for the frictional stress part include: dimensionless referential elastic modulus E_0, Poisson's ratio ν, and elastic constant controlling nonlinear stiffness n; parameters e_{ref}, Λ, and ξ for the evolution of critical void ratio; coefficients A_d and k_p depicting the nonlinear plastic hardening characteristics; parameters n_p and n_d depicting the stress dilatancy and shear softening. Basic parameters for the collisional part are: reference inertial ratio I_0,

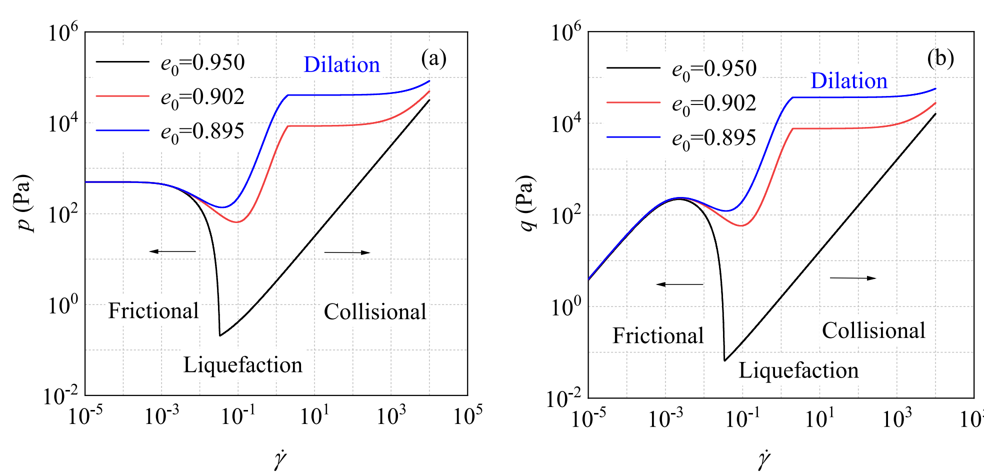

Fig. 11. Performance of the unified model in undrained simple shear tests with different void ratios (a) Relation between the hydrostatic stress and strain rate; (b) Relation between the deviatoric stress and strain rate.

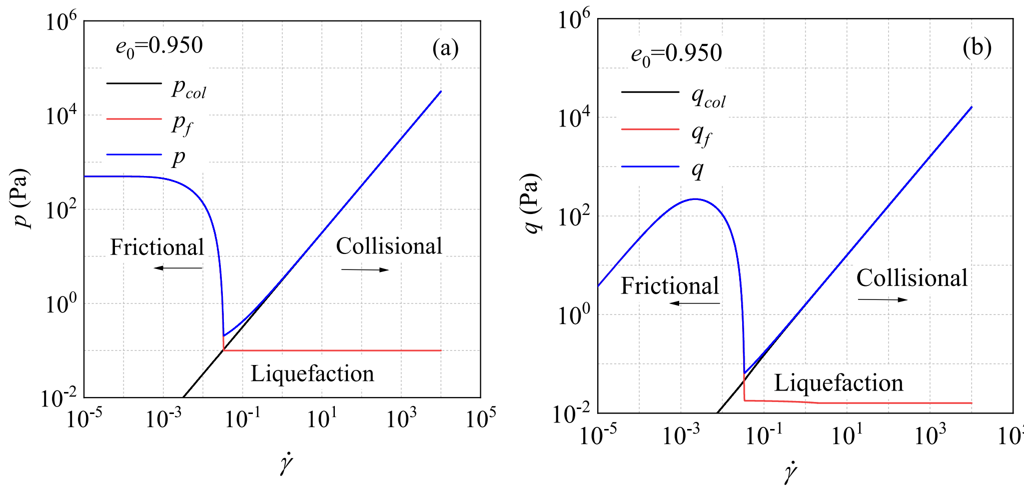

Fig. 12. Comparison of different types of hydrostatic and deviatoric stresses in the undrained simple shear test for the loose specimen with $e_0 = 0.950$: (a) Relation between the hydrostatic stress and strain rate; (b) Relation between the deviatoric stress and strain rate.

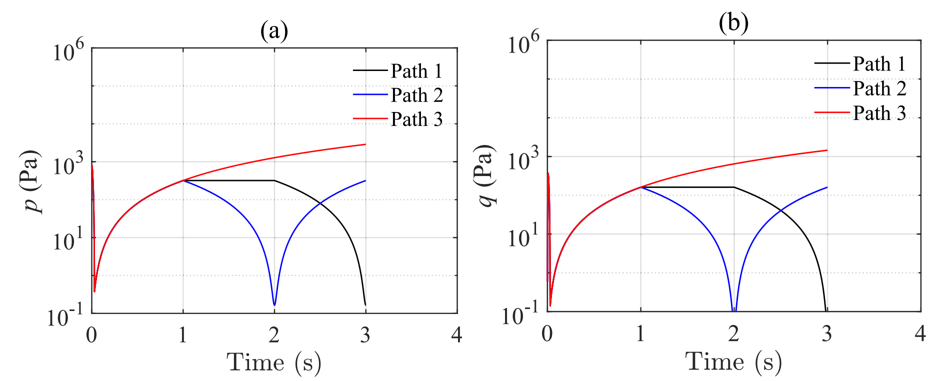

Fig. 13. Simulation results using the proposed elastoplasticity-(I) model with different strain rate paths ($e_0 = 0.950$) (a) relation between the hydrostatic stress and time; (b) relation between the deviatoric stress and time.

particle density ρ_s, particle diameter d, static friction coefficient μ_s, and dynamic friction coefficients μ_d for the $\mu(I)$ relation; random close volume fraction Φ_c and dynamic loosening factor $\Delta\Phi$ describing the influence of variable void ratio. Note that a detailed calibration process for these parameters is provided in Appendix C.

2.4.2. Element test simulation

To evaluate the effectiveness of the proposed unified phase transition model in depicting the granular flow from the solid-like to fluid-like state, element tests using the unified phase transition model are performed. The integration algorithm is the same as in Sections 2.2 and 2.3. The basic input parameters for the frictional and collisional part contributions are in Tables 2 and 3, respectively. Different initial void ratios $e_0 = 0.895$, 0.902, 0.950 are employed to distinguish different granular behaviours in large deformation flow. A fixed shear strain acceleration $\ddot{\gamma} = 50\text{s}^{-2}$ is adopted.

Fig. 11 illustrates the evolution of the total hydrostatic and deviatoric stress with different initial void ratios. Initially, in a solid-like state, all the samples are governed by frictional stress. As the strain rate increases, dense specimens tend to dilate. The frictional stress with the shear-hardening characteristic reaches the critical state to obtain a limited value. Meanwhile, collisional stress becomes more important at large strain rates, resulting in an increase in total stress. For the loose specimens (i.e., $e_0 = 0.950$), the initially dominant frictional stress with shear-softening behaviour reaches the critical state (i.e., liquefaction stage) to obtain the residual strength near zero. In the large strain rate regime, the collisional stress becomes dominant to control the viscous behaviour at the fluid-like state. These observations demonstrate that the proposed unified model can effectively depict the phase transition from a solid-like to a fluid-like state.

Considering the significance of the liquefaction phenomenon in depicting fast granular flow (e.g., debris flow and flow-like landslides), the hydrostatic and deviatoric components from total, frictional, and collisional stresses of the loose specimen with $e_0 = 0.950$ are derived and shown in Fig. 12. It shows that frictional stress is dominant in the solid-like state (i.e., at small strain rates), while collisional stress is the main controlling factor in the fluid-like state (i.e., at large strain rates). This indicates that the proposed unified model effectively satisfies the requirement of the phase transition model. Notedly, the individual critical-state-based elastoplastic sand model fails to capture the behaviour at the fluid-like state because it only has a small residual strength at large strain rate ranges.

The effect of the strain rate path on the proposed model is also examined. Samples with an initial void ratio e_0 of 0.95 are subjected to the different strain rate paths shown in Fig. 8. The simulation results are presented in Fig. 13. These results demonstrate that the frictional stress diminishes quickly, after which the collisional stress dominates. In the high strain rate regime, the collisional stress varies under different strain rate paths. Fig. 13 indicates that the developed solid-fluid phase transition model can effectively capture the strain acceleration dependence through the collisional stress component.

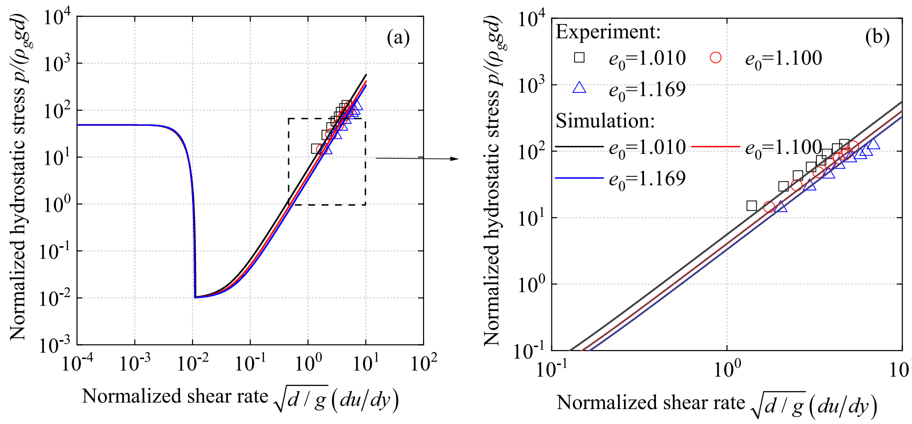

Fig. 14. Comparison of the hydrostatic stress from numerical and experimental results for polystyrene beads: (a) A wide range of shear rate from 10^{-4} to 10^{2}; (b) A small range of shear rate from 0.1 to 10.

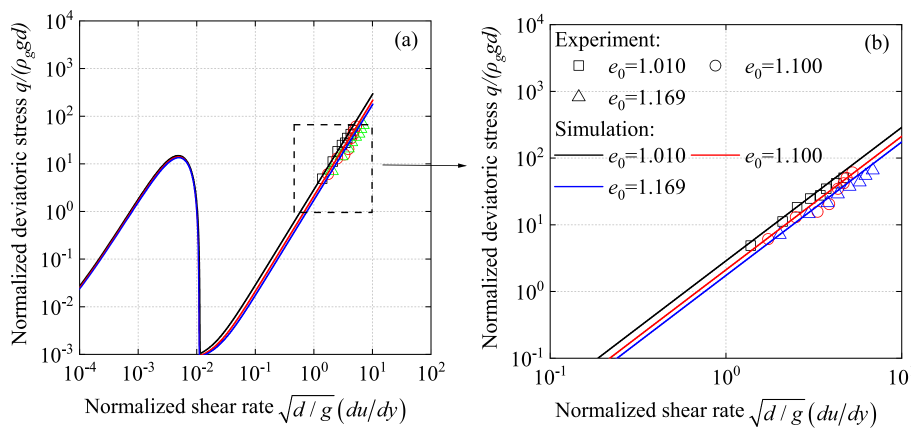

Fig. 15. Comparison of the deviatoric stress from numerical and experimental results for polystyrene beads: (a) A wide range of shear rate from 10^{-4} to 10^{2}; (b) A small range of shear rate from 0.1 to 10.

3. Verification of proposed phase transition model via element test

In this section, the performance of the proposed phase transition model will be evaluated against experiment results with two different granular materials by Savage and Sayed (1984).

3.1. Validation using polystyrene beads

Savage and Sayed (1984) investigated the response of granular materials such as polystyrene beads and glass beads using annular shear tests. In the prototype experiment, the volume of specimens remains constant, while a large shear strain rate is applied. Accordingly, the undrained simple shear test is employed to model the prototype experiment (Guo et al., 2016; Wang and Wu, 2024). According to the report by Guo et al. (2016), and Wang and Wu (2024), the initial pressure p_0 takes the value of 500 Pa. At the beginning, a shear rate of 10 s^{-1} and zero strain acceleration are given in 0.5 s, then a strain rate acceleration of 50 s^{-2} is applied from 0.5 s to 20 s. Note that we employ $\gamma = 0.5(\partial u/\partial y)$ when conducting simulation.

Table 4 lists the parameters for the polystyrene beads. According to Savage and Sayed (1984), Guo et al. (2016), and Wang and Wu (2024), the critical-state friction angle is 23°. The dimensionless referential elastic modulus is 190. The Possion's ratio is 0.235. The initial void ratios e_0 are 1.010, 1.100, and 1.169. The initial critical-state void ratio takes 0.910. The values of parameters Λ and ξ for the evolution of critical void ratio, coefficients A_d and k_p depicting the nonlinear plastic hardening characteristics, and parameters n_p and n_d for the stress dilatancy and shear softening are chosen for the typical granular material. The particle density in the prototype experiment was reported as $\rho_s = 1050$ kg/m^3. The diameter d is 1.0 mm. The static friction coefficient μ_s takes the values of $\tan\varphi = 0.4245$. The other parameters for the collisional part include reference inertial ratio I_0, dynamic friction coefficients μ_d, random close volume fraction Φ_c, and dynamic loosening factor $\Delta\Phi$ reported by Wang and Wu (2024) are employed.

Figs. 14 and 15 depict the normalized hydrostatic stress-shear rate and normalized deviatoric stress-shear rate relations under the logarithm coordinate, respectively. It demonstrates that the proposed phase transition model can well approximate the measured response from the experiment results. From the solid-like to fluid-like state, the total hydrostatic and deviatoric stresses first decrease in the small strain rate range and then increase in the large strain rate range. This is because the dominant stress changes from frictional to collisional stress. These observations validate the developed phase transition model.

3.2. Validation using glass beads

To further demonstrate the applicability of the proposed phase transition model in depicting the behaviour of granular flow, element tests of the glass beads are utilized. The initial pressure and loading strain rate path are the same as those used for the polystyrene beads. The parameters for the glass beads are listed in Table 4. According to Savage and Sayed (1984), Guo et al. (2016), and Wang and Wu (2024), the critical-state friction angle is 25°. The dimensionless referential elastic

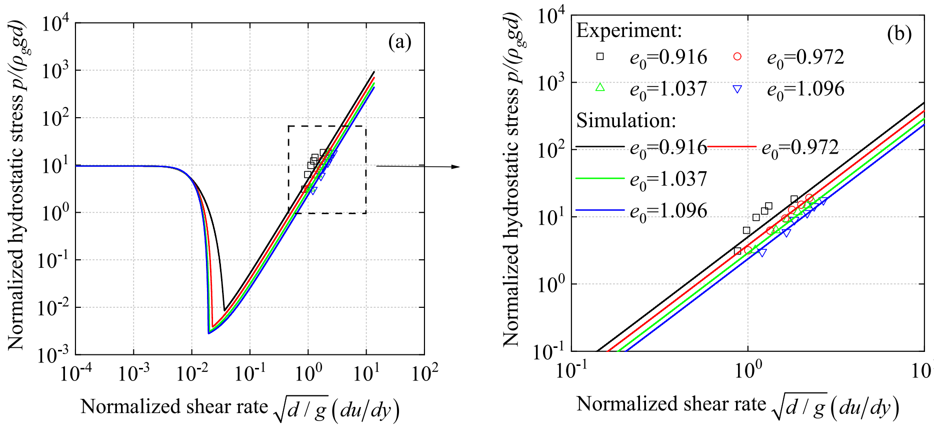

Fig. 16. Comparison of the hydrostatic stress from numerical and experimental results for glass beads: (a) A wide range of shear rate from 10^{-4} to 10^2; (b) A small range of shear rate from 0.1 to 10.

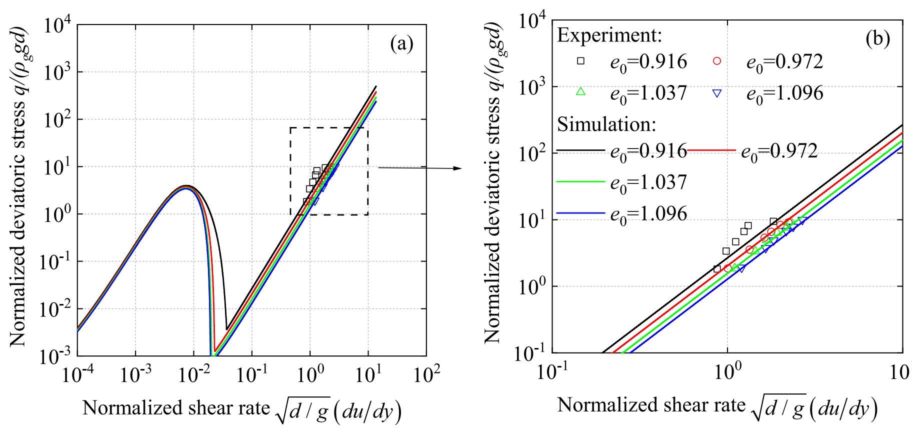

Fig. 17. Comparison of the deviatoric stresses from numerical and experimental results for glass beads: (a) A wide range of shear rate from 10^{-4} to 10^2; (b) A small range of shear rate from 0.1 to 10.

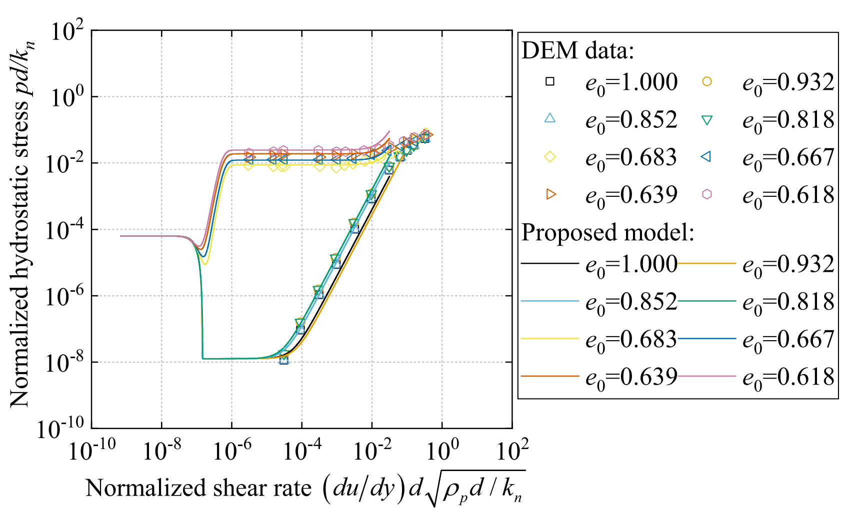

Fig. 18. Comparison of the hydrostatic stress from numerical solutions and DEM results by Chialvo et al. (2012).

modulus is 200. The Possion's ratio is 0.235. Four different void ratios $e_0 = 0.916$, 0.972, 1.037, and 1.096 are employed. The initial critical-state void ratio is 0.917. The particle density in the prototype experiment was reported as $\rho_s = 2970$ kg/m^3. The diameter d is 1.8 mm. The static friction coefficient μ_s takes the values of $\tan\varphi = 0.4660$. The other parameters for the frictional and collisional parts take typical values for granular material (see Table 4).

Figs. 16 and 17 depict the normalized hydrostatic stress-shear rate and normalized deviatoric stress-shear rate relations for the glass beads, respectively. This comparison once again emphasizes the proposed phase transition model's capacity to reasonably approximate laboratory element tests. The proposed phase transition model can effectively

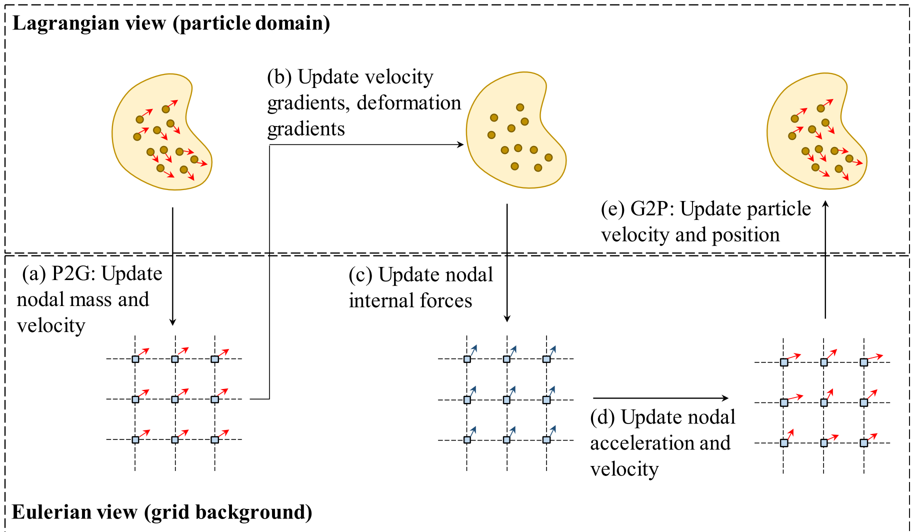

Fig. 19. Illustration of the material point method solution algorithm.

describe the evolution of stress in granular flow from a solid-like to a fluid-like state.

3.3. Validation using DEM results

To further validate the effectiveness of the proposed phase transition model, the DEM results from Chialvo et al. (2012) are utilized. In the DEM simulations, a simple shear test under constant volume conditions is performed. Accordingly, an undrained simple shear test is adopted in this study. The parameters employed are listed in Table 4. The critical-state friction angle is set to 21.11°, as reported by Vescovi et al. (2020a, 2020b). The dimensionless referential elastic modulus and Poisson's ratio are set to 200 and 0.235, respectively. Other parameters are not explicitly reported and are therefore assigned typical values for granular media based on Yin et al. (2020). The void ratios considered include e_0 = 1.000, 0.932, 0.852, 0.818, 0.683, 0.667, 0.639, and 0.618, as reported in Chialvo et al. (2012). The basic simulation conditions are consistent with those described in subsection 3.1.

Fig. 18 illustrates the simulation results obtained using the proposed elastoplasticity-$\mu(I)$ model alongside the DEM data from Chialvo et al. (2012). The DEM results depict the stress evolution under a smaller strain rate compared to the figures in subsections 3.1 and 3.2. The proposed phase transition model aligns well with the DEM data, further validating its effectiveness in capturing the stress-strain relationship under both high and low strain rates regimes.

4. Application of the proposed phase transition model via MPM

In this section, the validated elastoplasticity-$\mu(I)$ phase transition model will be integrated into the material point method to address boundary value problems, including 2D granular slumping and 3D cylindrical granular collapse, thereby evaluating its effectiveness in simulating large deformation granular flow.

4.1. Material point method

MPM is a numerical approach that combines Eulerian (stationary backdrop grid) and Lagrangian (material points) descriptions. Material properties such as velocity, displacement, tension, and strain are stored at Lagrangian material points, while the governing equations are solved on an Eulerian grid. Shape functions facilitate the transfer of information between the Lagrangian material points and the Eulerian grid. In MPM, the mass conservation equation is inherently satisfied, with the momentum conservation equation serving as the primary equation to be solved, as follows:

$$\rho\dot{\mathbf{v}} = \nabla\cdot\boldsymbol{\sigma} + \rho\mathbf{b} \tag{19}$$

where ρ is the density; $\mathbf{v}$ denotes the velocity; $\dot{\square}$ is the notation for the time derivative; ∇ is the gradient operator; $\boldsymbol{\sigma}$ is the Cauchy stress tensor, and $\mathbf{b}$ is the body force.

The strong form of Eq. (19) can be converted to its weak form by multiplying it with a test function, and the resulting weak form of the conservation equation can be integrated by parts over the material domain. The derivation of the MPM solution scheme is beyond the scope of this work; therefore, only the final fully discretized and linearized solution scheme is presented, with further details available in Liang et al. (2024).

The calculation processes at each time step of the MPM solution algorithm are summarized below (see Fig. 19):

(a) Particle to Grid (i.e., P2G): At the current step t^k, update the nodal mass m_I^k and nodal velocity $\mathbf{v}_I^k$:$m_I^k = \sum_p N_{Ip}^k m_p$, $\mathbf{v}_I^k = \left(\sum_p N_{Ip}^k m_p \mathbf{v}_p^k\right)/m_I^k$ (where $N_{Ip}^k = N_I\left(\mathbf{x}_p^k\right)$ is the shape function; m_p and $\mathbf{v}_p^k$ are the mass and velocity of the particle).

(b) Update the particle velocity gradient $\nabla\mathbf{v}_p^k$ and deformation gradient $\mathbf{F}_p^k$: $\nabla\mathbf{v}_p^k = \sum_I \nabla N_{Ip}^k \mathbf{v}_I^k$, $\mathbf{F}_p^k = \left(1 + \nabla\mathbf{v}_p^k\Delta t\right)\mathbf{F}_p^{k-1}$.

(c) Update nodal internal forces $\mathbf{f}_I^{int,k}$: $\mathbf{f}_I^{int,k} = -\sum_p \boldsymbol{\sigma}_p^k\cdot\nabla N_{Ip}^k V_p^k$. Note that the nodal external force$\mathbf{f}_I^{ext,k}$ only considers the gravity in the typical granular flow.

(d) Update nodal acceleration $\mathbf{a}_I^k$ and velocity $\mathbf{v}_I^{k+1}$: $\mathbf{a}_I^k = \left(\mathbf{f}_I^{int,k} + \mathbf{f}_I^{ext,k}\right)/m_I^k$, $\mathbf{v}_I^{k+1} = \mathbf{v}_I^k + \mathbf{a}_I^k\Delta t$.

(e) Grid to Particle (G2P): update the particle velocity $\mathbf{v}_p^{k+1}$ and position $\mathbf{x}_p^{k+1}$: $\mathbf{v}_p^{k+1} = \mathbf{v}_p^k + \sum_I \mathbf{a}_I^k N_{Ip}^k\Delta t$, $\mathbf{x}_p^{k+1} = \mathbf{x}_p^k + \sum_I \mathbf{v}_I^{k+1} N_{Ip}^k\Delta t$.

The steps (a-e) form a basic loop in MPM simulation. For the next time step, the background grid information is discarded to maintain the grid node positions unchanged. It is important to note that the proposed unified elastoplasticity-$\mu(I)$ model is implemented in Step (c) when calculating the nodal internal forces.

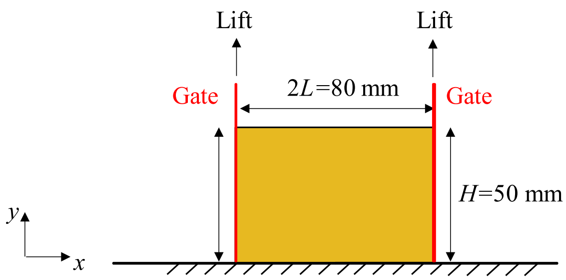

Fig. 20. Illustration of 2D granular flow with two free surfaces.

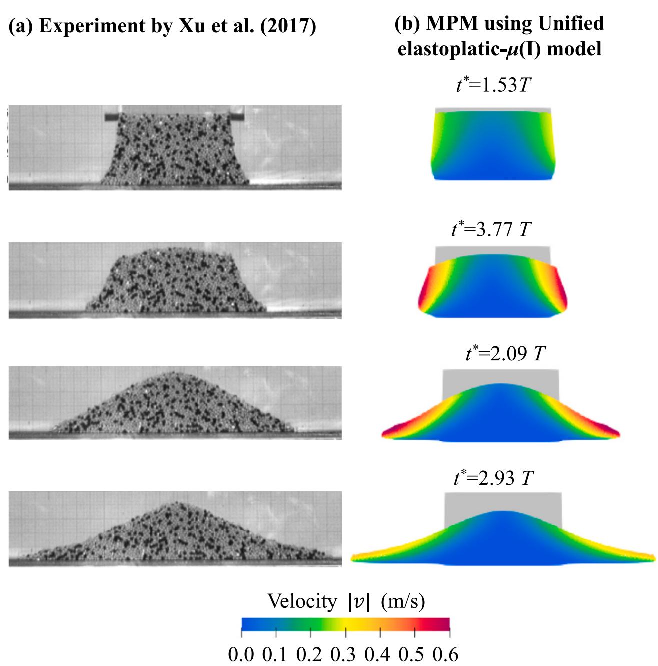

Fig. 21. Free surface for granular flow between MPM results unified elastoplasticity-$\mu(I)$ model and experimental results by Xu et al. (2017) (length unit: cm).

4.2. Case 1: 2D granular slumping

4.2.1. Model setup

To validate the proposed elastoplasticity-$\mu(I)$ model, we first utilized the experimental results of 2D granular slumping on a horizontal surface from Xu et al. (2017). Initially, glass beads were packed into a column, remaining in a solid-like state. Upon the sudden release of gates on both sides, the material transitioned to a fluid-like state, producing granular flow.

Fig. 20 illustrates the initial geometry of the column, with a height H of 50 mm and a length 2 L of 80 mm, resulting in a length-to-height ratio of 1.25. The MPM simulation is set up under identical experimental conditions. For simplicity, the gate-lifting process is not simulated. As base layer friction has a negligible effect on the collapse (Fern and Soga, 2016), a no-slip boundary condition is applied to the base. The computational domain is discretized into square elements with a grid size of 2 mm, and the initial spacing between material points (MPs) is set to 0.5 mm, yielding a total of 64,000 MPs. To ensure stability and accuracy, a time step of $\mathrm{dt} = 1 \times 10^{-6}$ s is used, and a total time of 0.5 s is simulated.

Table 4 lists the parameters for the elastoplasticity-$\mu(I)$ model. For the elastoplastic stress, the dimensionless referential elastic modulus E_0, Poisson's ratio ν, and constant controlling nonlinear stiffness n are set to 150, 0.2, and 0.5, respectively. The friction angle φ is reported as 20.9°

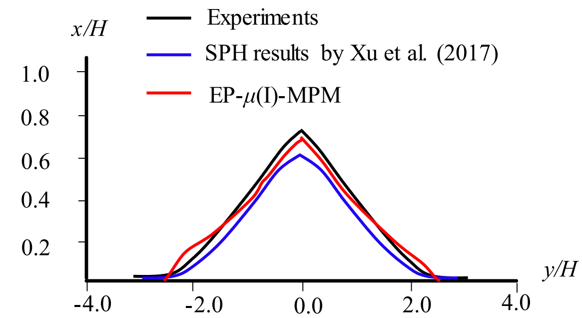

Fig. 22. Comparison of free surface for granular flow at $t^* = 5.88\ T$ between EP-$\mu(I)$-MPM results, EP-MPM results, experimental results by Xu et al. (2017), and SPH solutions by Xu et al. (2017).

(Franci and Cremonesi, 2019). Other parameters are based on typical values reported by Yin et al. (2018). For the viscous stress parameters, the glass beads used in the study have the following properties according to Franci and Cremonesi (2019): $\rho_\mathrm{d} = 2500$ kg/m^3, $\mu_s = \tan(20.9^\circ) = 0.382$, $\mu_d = 0.643$, $I_0 = 0.279$. Additional material properties, including particle diameter $d = 1$ mm, random close volume fraction Φ_c=0.70, and dynamic loosening factor $\Delta\Phi$=0.29 are taken from Wang and Wu (2024). Note that accurately determining all the parameters of the proposed solid-fluid phase transition model is challenging, and this can be considered a limitation of the current study.

4.2.2. Simulation results

Fig. 21 compares the numerical and experimental results at four different time instants. A constant lifting velocity of $v_L = 0.56$ m/s is assumed (Franci and Cremonesi, 2019), corresponding to a lifting duration of 0.09 s. The experimental results at the reference time $t^* = t/\sqrt{g/H}$ (where $g = 9.81$ m/s^2) correspond to the simulation results at $t^* - 0.09$ s. The figure shows a good agreement between the MPM simulation results using the unified elastoplasticity-$\mu(I)$ constitutive model and the experimental data, demonstrating the accuracy of the proposed unified elastoplasticity-$\mu(I)$ model.

Fig. 22 further presents the final granular flow positions as determined by the MPM simulation using the proposed unified elastoplasticity-$\mu(I)$ model in this study, experimental data from Xu et al. (2017), and SPH results from the same source. The comparison demonstrates that both MPM and SPH continuum simulations align well with the experimental outcomes. Notably, the MPM simulation, utilizing the proposed elastoplasticity-$\mu(I)$ model, more accurately predicts the deposition height compared to the SPH simulation, further highlighting the effectiveness of the proposed model.

To analyze the unified elastoplasticity-$\mu(I)$ model, the evolution of two key variables is examined (see Fig. 23): the equivalent plastic strain ϵ^p_{eff} from the solid-like critical-state-based elastoplastic model, and the equivalent shear viscosity $\eta = 2f_\Phi\mu|\dot{\gamma}|$ from the fluid-like viscous $\mu(I)$ model. The equivalent plastic strain effectively delineates the boundary between solid-like particles in the small-strain regime and fluid-like particles in the large-strain rate regime. Meanwhile, the equivalent shear viscosity captures the evolution of viscous stress. Fig. 23(b1)-(b4) show the evolution of equivalent shear viscosity η during the granular flow, indicating that the viscosity of the mobilized particles initially rises from zero, then decreases back to zero. This behaviour clearly illustrates the transition of dominant stress from elastoplastic stress to elastoplastic-viscous stress, and finally back to elastoplastic as the material transitions from a solid-like to fluid-like state, and back to a solid-like state, effectively validating the proposed elastoplasticity-$\mu(I)$ model.

Specifically, Fig. 23(a1)-(a2) illustrate the initiation of granular flow due to plastic failure, where particles in this region experience significant deformation, as indicated by equivalent plastic strain values approaching 1.0. Concurrently, viscous stress begins to develop, as

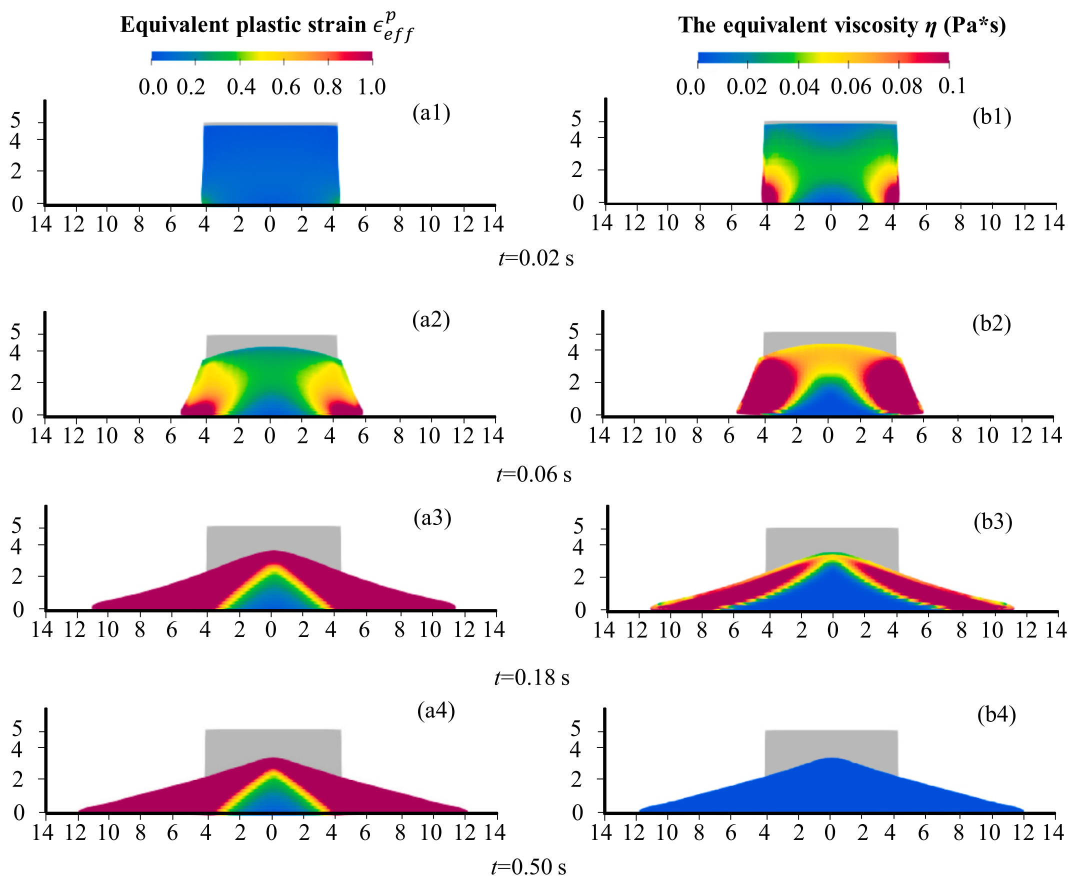

Fig. 23. The evolution of the equivalent plastic strain ϵ_{eff}^{p} and equivalent viscosity η in this study (length unit: cm).

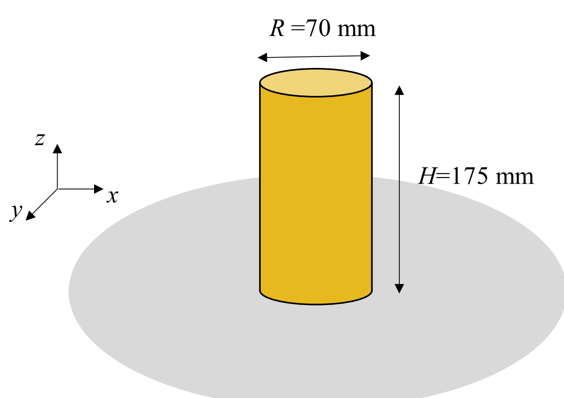

Fig. 24. Illustration of 3D cylindrical granular flow.

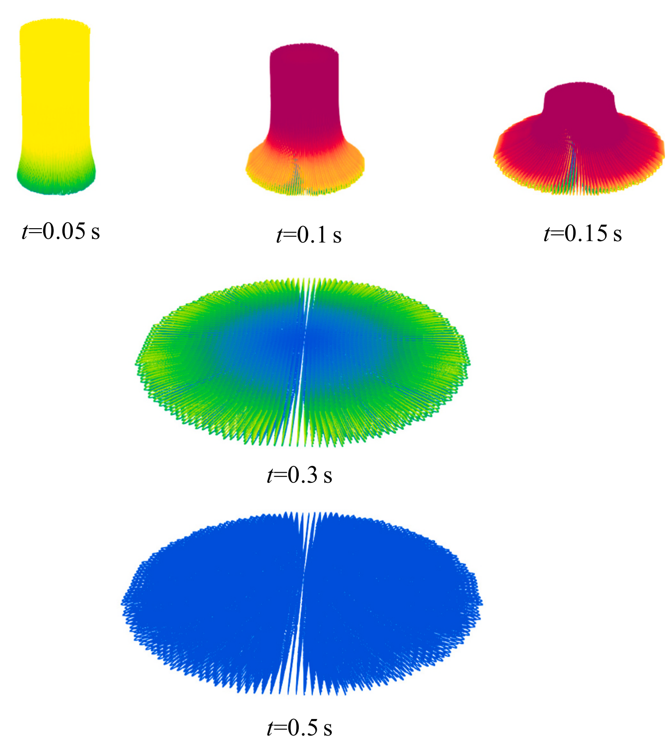

Fig. 25. Velocity contours in 3D cylindrical granular column collapse.

represented by equivalent shear viscosity (see Fig. 23(b1)-(b2)). Fig. 23 (a3) further distinguishes between the mobilized zone, where material points reach the critical state and exhibit fluid-like behaviour, and the solid-like zone, where material points remain unchanged. The interface between these zones marks the transition from solid-like to fluid-like behaviour. In the solid-like state, elastoplastic stress predominantly governs the material, as evidenced by the absence of equivalent shear viscosity. Conversely, in the fluid-like zone, both elastoplastic and viscous stresses are present (see Fig. 23(b3)), with the increase in shear viscosity associated with rapid granular flow. Ultimately, the flow ceases due to basal friction (see Fig. 23(a4) and (b4)), with equivalent shear viscosity decreasing to zero, signifying a return to frictional stress dominance. These observations confirm that the proposed unified elastoplasticity-$\mu(I)$ model effectively captures the solid-like behaviour

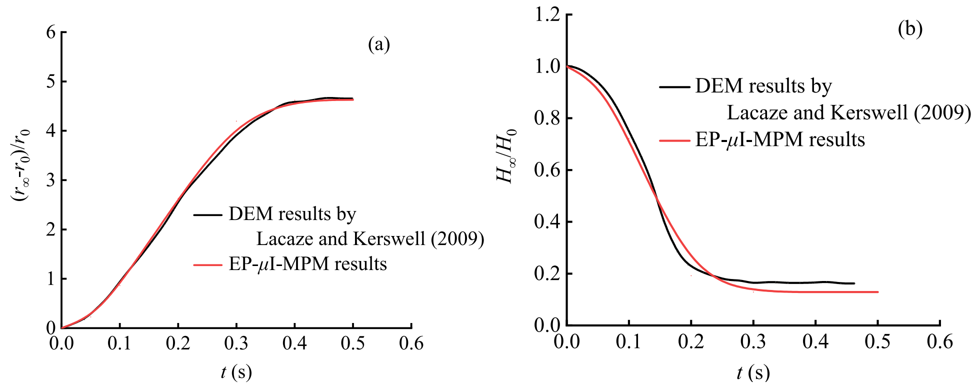

Fig. 26. Comparison of the time evolution of dimensionless radius variation and height variation from DEM and MPM simulation using unified elastoplasticity-$\mu(I)$ constitutive model: (a) dimensionless radius variation $(r_\infty - r_0)/r_0$; (b) dimensionless residual height variation (h_∞/H_0).

during the inception and deposition stages and the fluid-like behaviour during the propagation phase.

4.3. Case 2: 3D cylindrical granular collapse

4.3.1. Model setup

This section employs a 3D cylinder granular flow by Lacaze and Kerswell (2009) to demonstrate the wider application of the validated MPM model with the unified elastoplasticity-$\mu(I)$ constitutive model. The initial cylinder has a height H of 175 mm and a diameter R of 70 mm (see Fig. 24). In the MPM model, the no-slip condition is adopted for the bottom boundary for simplicity. The computational domain is discretized with cubic elements using the grid size of 8 mm, and each grid housing 36 material points, yielding a total of 284,724 MPs for the simulation. To ensure the stability and accuracy of the simulation, the time step $\mathrm{dt} = 1 \times 10^{-6}$ s is employed. A total time of 0.5 s is simulated. The material parameters of Lacaze and Kerswell (2009) for the elastoplasticity-$\mu(I)$ model are listed in Table 4. These parameters are not discussed for simplicity, the details can be referred to Franci and Cremonesi (2019).

4.3.2. Simulation results

Fig. 25 demonstrates the evolution of the velocity magnitude in 3D granular flow. Initially, the top of the cylindrical granular pile undergoes near free-fall under gravity, while the base starts to move laterally, with the elastoplastic stress arriving at the critical state (see $t = 0.05$ s). Subsequently, the heap transitions into a fluid-like state governed by both elastoplastic and viscous stresses, as observed at $t =$ 0.1 s and 0.15 s. Before halting, only a narrow layer near the free surface of the granular mass continues to move gradually. Finally, all particles cease movement and return to a solid-like state.

Fig. 26 further depicts the evolution in time of the dimensionless radius $(r_\infty - r_0)/r_0$ and residual height (h_∞/H_0) (where r_∞ and r_0 are the deposition radius and initial radius, respectively; h_∞ and H_0 are the deposition radius and initial radius, respectively) obtained with the proposed MPM scheme using unified elastoplasticity-$\mu(I)$ constitutive model and the DEM results by Lacaze and Kerswell (2009). The comparison reveals good agreement between the continuum and discrete numerical solutions. Notably, the curve in Fig. 26(a) maintains a constant slope between 0.05 s and 0.35 s, consistent with the granular flow experimental findings by Lube et al. (2004). These observations demonstrate the robust capability of the EP-$\mu(I)$-MPM model to accurately simulate 3D granular flow.

5. Conclusions

This study has proposed a novel unified elastoplasticity-$\mu(I)$ phase transition constitutive model (EP-$\mu(I)$) and implemented it into the material point method (MPM) numerical scheme, which accurately simulates large deformation granular flow by capturing the solid-like behaviour during the inception and deposition stages and fluid-like behaviour during propagation. Based on the generalized Maxwell framework, the proposed unified elastoplasticity-$\mu(I)$ constitutive model integrates an elastoplastic stress and a viscous $\mu(I)$ stress, encompassing key features such as nonlinear elasticity, nonlinear plastic hardening, stress dilatancy, and critical-state principle, while the viscous stress is dependent on both strain rate and strain acceleration. Implemented within the MPM framework (EP-$\mu(I)$-MPM), this model has been validated through simulations of both 2D and 3D granular flows. Key findings include:

1. The elastoplasticity part is established to consider the nonlinear elasticity, dilatancy (contraction or dilation), nonlinear plastic hardening, and the critical state in the solid-like state during granular flow. Based on the element test simulation, it is indicated that this elastoplastic part can effectively describe the dependence on the void ratio and the initiation of granular flow.
2. The $\mu(I)$ rheology part is established to consider the dependence on the void ratio, strain rate, and strain acceleration in the fluid-like state during granular flow. Element test simulation results indicate this part can efficiently depict these dependencies and the propagation of granular flow.
3. By comparing the element test simulation results with experimental data, it is evident that the proposed phase transition model effectively describes the phase transition of granular media from a solid-like state during the initiation stage to a fluid-like state during the propagation stage.
4. The MPM numerical simulations for 2D and 3D granular flows demonstrate remarkable consistency with experimental data, emphasizing the effectiveness of the proposed elastoplasticity-$\mu(I)$ constitutive model.
5. The proposed EP-$\mu(I)$-MPM successfully captures the solid-like and fluid-like characteristics across different stages of granular flow: during initiation, propagation, and deposition, the dominant stress transitions from elastoplastic to elastoplastic-viscous and ultimately to elastoplastic, reflecting the material's shift from a solid-like state to a fluid-like state and back to a solid-like state. Specifically, the initiation of granular flow is described using the critical state in the proposed elastoplasticity-$\mu(I)$ constitutive model.

CRediT authorship contribution statement

Hang Feng: Writing – review & editing, Writing – original draft, Validation, Formal analysis, Data curation. **Zhen-Yu Yin:** Writing – review & editing, Investigation, Funding acquisition, Data curation, Conceptualization. **Weijian Liang:** Writing – review & editing, Supervision.

Declaration of competing interest

The authors declare that they have no known competing financial interests or personal relationships that could have appeared to influence the work reported in this paper.

Acknowledgements

This work was supported by the general research fund of the Research Grants Council (RGC) of the Hong Kong Special Administrative Region Government (HKSARG) of China (grant No. 15232224, 15229223).

Appendix A. The undrained simple shear test

In the simple shear test, the specimen is laterally confined with two plates at the top and bottom. The top plate moves horizontally to generate the shear deformation. Under the simple shear condition, the stress tensor is expressed as follows:

$$\sigma = \begin{bmatrix} \sigma_{xx} & \tau_{xy} & 0 \\ \tau_{yx} & \sigma_{yy} & 0 \\ 0 & 0 & \sigma_{zz} \end{bmatrix} = \begin{bmatrix} \sigma_n & \tau_{xy} & 0 \\ \tau_{yx} & \sigma_n & 0 \\ 0 & 0 & \sigma_n \end{bmatrix} \tag{A1}$$

where σ_n is the vertical stress; τ_{xy} is the shear stress. Accordingly, the hydrostatic and deviatoric parts of the stress are express as: $p = \sigma_n$ and $q = \tau_{xy}$, respectively.

The strain tensor is expressed as:

$$\varepsilon = \begin{bmatrix} \varepsilon_{xx} & \varepsilon_{xy} & 0 \\ \varepsilon_{yx} & \varepsilon_{yy} & 0 \\ 0 & 0 & \varepsilon_{yy} \end{bmatrix} = \begin{bmatrix} \varepsilon_n & \gamma & 0 \\ \gamma & \varepsilon_n & 0 \\ 0 & 0 & \varepsilon_n \end{bmatrix} \tag{A2}$$

where ε_n is the vertical strain. γ is the shear strain. The volumetric and deviatoric parts of the strain are express as: $\varepsilon_v = \varepsilon_n$ and $\varepsilon_d = \gamma$, respectively. In the undrained simple test, the volumetric strain is zero, i.e., $\varepsilon_v = \varepsilon_n = 0$. p_f and q_f are employed to denote the vertical stress and shear stress of the frictional stress part, respectively. p_{col} and q_{col} are used to denote the vertical stress and shear stress of the collisional stress part, respectively. γ is used to denote the shear strain.

Appendix B. Collisional stress part in the undrained simple test

The strain rate tensor in the undrained simple test is expressed as:

$$\dot{e} = \begin{bmatrix} 0 & \dot{\varepsilon}_{xy} & 0 \\ \dot{\varepsilon}_{yx} & 0 & 0 \\ 0 & 0 & 0 \end{bmatrix} = \begin{bmatrix} 0 & \dot{\gamma} & 0 \\ \dot{\gamma} & 0 & 0 \\ 0 & 0 & 0 \end{bmatrix} \tag{B1}$$

The strain acceleration tensor in the undrained simple test is expressed as:

$$\ddot{e} = \begin{bmatrix} 0 & \ddot{\varepsilon}_{12} & 0 \\ \ddot{\varepsilon}_{21} & 0 & 0 \\ 0 & 0 & 0 \end{bmatrix} = \begin{bmatrix} 0 & \ddot{\gamma} & 0 \\ \ddot{\gamma} & 0 & 0 \\ 0 & 0 & 0 \end{bmatrix} \tag{B2}$$

The first part of the collisional stress in the undrained simple test is expressed as:

$$2\mu|\dot{\gamma}|\ddot{e} = \begin{bmatrix} 0 & 2\mu|\dot{\gamma}|\ddot{\gamma} & 0 \\ 2\mu|\dot{\gamma}|\ddot{\gamma} & 0 & 0 \\ 0 & 0 & 0 \end{bmatrix} \tag{B3}$$

The second part of the collisional stress in the undrained simple test is expressed as:

$$\dot{\mathbf{e}}\ddot{\mathbf{e}} = \begin{bmatrix} 0 & \dot{\varepsilon}_{12} & 0 \\ \dot{\varepsilon}_{21} & 0 & 0 \\ 0 & 0 & 0 \end{bmatrix} \cdot \begin{bmatrix} 0 & \ddot{\varepsilon}_{12} & 0 \\ \ddot{\varepsilon}_{21} & 0 & 0 \\ 0 & 0 & 0 \end{bmatrix} = \begin{bmatrix} \dot{\varepsilon}_{12}\ddot{\varepsilon}_{21} & 0 & 0 \\ 0 & \dot{\varepsilon}_{21}\ddot{\varepsilon}_{12} & 0 \\ 0 & 0 & 0 \end{bmatrix} = \begin{bmatrix} \dot{\gamma}\ddot{\gamma} & 0 & 0 \\ 0 & \dot{\gamma}\ddot{\gamma} & 0 \\ 0 & 0 & 0 \end{bmatrix} \tag{B4}$$

The third part of collisional stress in the undrained simple test is expressed as:

$$\ddot{\mathbf{e}}\dot{\mathbf{e}} = \begin{bmatrix} 0 & \ddot{\varepsilon}_{12} & 0 \\ \ddot{\varepsilon}_{21} & 0 & 0 \\ 0 & 0 & 0 \end{bmatrix} \cdot \begin{bmatrix} 0 & \dot{\varepsilon}_{12} & 0 \\ \dot{\varepsilon}_{21} & 0 & 0 \\ 0 & 0 & 0 \end{bmatrix} = \begin{bmatrix} \ddot{\varepsilon}_{12}\dot{\varepsilon}_{21} & 0 & 0 \\ 0 & \ddot{\varepsilon}_{21}\dot{\varepsilon}_{12} & 0 \\ 0 & 0 & 0 \end{bmatrix} = \begin{bmatrix} \ddot{\gamma}\dot{\gamma} & 0 & 0 \\ 0 & \ddot{\gamma}\dot{\gamma} & 0 \\ 0 & 0 & 0 \end{bmatrix} \tag{B5}$$

By adding Eqs.(B3) ~ (B5), the collisional stress rate is expressed as follows:

$$\dot{\sigma}_{col} = f_\Phi(2\mu|\dot{\gamma}|\ddot{\mathbf{e}} - \dot{\mathbf{e}}\ddot{\mathbf{e}} - \ddot{\mathbf{e}}\dot{\mathbf{e}}) = f_\Phi \begin{bmatrix} -2\dot{\gamma}\ddot{\gamma} & 2\mu|\dot{\gamma}|\ddot{\gamma} & 0 \\ 2\mu|\dot{\gamma}|\ddot{\gamma} & -2\dot{\gamma}\ddot{\gamma} & 0 \\ 0 & 0 & 0 \end{bmatrix} \tag{B6}$$

Accordingly, the hydrostatic and deviatoric part of the collisional stress rate is expressed as:

$$\dot{p}_{col} = -2f_{\Phi}\dot{\gamma}\ddot{\gamma} \tag{B7}$$

$$\dot{q}_{col} = 2\mu f_{\Phi}|\dot{\gamma}|\ddot{\gamma} \tag{B8}$$

Appendix C. Calibration for the proposed unified elastoplasticity-$\mu(I)$ model

For the proposed unified elastoplasticity-$\mu(I)$ model, 19 parameters are required, as shown in the Table 4. Determining the input parameters for different materials will be divided into 2 parts:

Part 1: The first part is determining the parameters of the elastoplasticity-based frictional stress model, which has the following 4 steps:

- Step 1–1: Determination of CSL parameters of e_{ref}, Λ, and ξ.

To determine the parameters of e_{ref}, Λ, and ξ, triaxial tests are conducted to obtain the CSL. In the CSL, the parameter e_{ref} is the reference void ratio corresponding to the mean effective frictional stress is zero; the parameter Λ controls the slope of the CSL; the parameter ξ controls the position of the inflection point in the CSL.

- Step 1–2: Determination of elastic parameters of E_0, ν, and n.

Parameter ν can be obtained through data from triaxial tests by plotting the axial strain versus radial strain and determining ν from the slope of the line. Additionaly, this parameter can also determined from the literature, as suggested by Yin et al. (2020), ranges from 0.2 to 0.25. Parameters E_0 and n can be obtained from isotropic compression tests. The parameter n usually takes the value of 0.5–0.7, as suggested by Yin et al. (2020).

- Step 1–3: Determination of parameters φ_c and e_0.

Critical angle φ_c can take the value from the drained direct shear test or drained triaxial test. Parameter e_0 is the initial void ratio provided by the triaxial test.

- Step 1–4: Determination of parameters A_d, k_{p}, n_p, and n_d.

These four parameters can be derived from undrained or drained triaxial tests. As suggested by Yin et al. (2020), both n_p and n_d can take the value of 1 when direct determination of these parameters is challenging. Parameter A_d can take the value of 0.5–1.5, while k_p usually takes the value from 0.0001 to 0.01.

Part 2: The second part is determining the parameters of the modified $\mu(I)$ rheology model, which has the following 2 steps:

- Step 2–1: Determination of parameters of ρ_s, d, and μ_s.

Parameter $\boldsymbol{\rho_s}$ and d can be determined via the laboratory test. These two parameters are also determined from the literature. Parameter $\boldsymbol{\mu_s}$ takes the value of $\tan\varphi_c$.

- Step 2–2: Determination of parameters of elastic parameters I_0, μ_d, Φ_{c}, and $\Delta\Phi$.

DEM simulation, undrained simple shear test, or the annular shear test, can be employed to obtain the $\mu(I)$ relation, further obtaining the $\boldsymbol{\mu_d}$ and $\boldsymbol{I_0}$. The stress-shear rate relation in the undrained simple shear test can be employed to obtain $\boldsymbol{\Phi_c}$ **and** $\Delta\Phi$.

While determining the optimal value of these parameters, the machine learning algorithm can serve as a reliable tool, which has been discussed in our group (see Jin et al., 2016; Jin et al., 2017).

Data availability

Data will be made available on request.

References

Alaei, E., Marks, B., Einav, I., 2021. A hydrodynamic-plastic formulation for modelling sand using a minimal set of parameters. J. Mech. Phys. Solids 151, 104388.
Bagnold, R.A., 1954. Experiments on a gravity-free dispersion of large solid spheres in a Newtonian fluid under shear. Proc. Royal Soc. London. Series A. Math. Phys. Sci. 225 (1160), 49–63.
Baumgarten, A.S., Kamrin, K., 2019. A general fluid–sediment mixture model and constitutive theory validated in many flow regimes. J. Fluid Mech. 861, 721–764.
Berzi, D., Vescovi, D., Ji, S., Li, X., Luding, S., 2022. Flow regimes and phase transitions in granular matter: Multiscale modeling from micromechanics to continuum-editorial. Granul. Matter 24 (1), 3.
Cheng, W., Yin, Z.-Y., 2024. Fractional order viscoplastic modeling of anisotropically overconsolidated clays with modified isotach viscosity. Int. J. Plast. 172.
Cheng, W., Chen, R.-P., Yin, Z.-Y., Wang, H.-L., Meng, F.-Y., 2023. A fractional-order two-surface plasticity model for over-consolidated clays and its application to deep gallery excavation. Comput. Geotech. 159, 105494.
Chialvo, S., Sun, J., Sundaresan, S., 2012. Bridging the rheology of granular flows in three regimes. Phys. Rev. E-Stat. Nonlinear Soft Matter Phys. 85 (2), 021305.
Di Carluccio, G., Pinyol, N.M., Alonso, E.E., Hürlimann, M., 2022. Liquefaction-induced flow-like landslides: the case of Valarties (Spain). Géotechnique 74 (4), 307–324.
Dikau, R., Commission E, 1996. Landslide Recognition: Identification, Movement, and Clauses.
Dunatunga, S., Kamrin, K., 2015. Continuum modelling and simulation of granular flows through their many phases. J. Fluid Mech. 779, 483–513.
Dutto, P., 2014. Modelling of Landslides Propagation with SPH: Effects of Rheology and Pore Water Pressure (Doctoral dissertation,Caminos).
Feng, H., Huang, M., Shi, Z., Shen, K., Wang, B., 2024. Macro-element modeling of suction caisson subjected to vertical tensile loading via up-scaling soil stress-strain relations. Ocean Eng. 304, 117850.
Feng, H., Liang, W., Yin, Z.Y., Hu, L., 2025. Material Point Method Modeling of Granular Flow Considering Phase Transition From Solid-like to Fluid-like States. Int. J. Numerical Anal. Methods Geomech 49 (6), 1642–1664.
Fern, E.J., Soga, K., 2016. The role of constitutive models in MPM simulations of granular column collapses. Acta Geotechnica 11 (3), 659–678.

Franci, A., Cremonesi, M., 2019. 3D regularized μ(I)-rheology for granular flows simulation. J. Comput. Phys. 378, 257–277.
Gajo, A., Wood, M., 1999. Severn–Trent sand: a kinematic-hardening constitutive model: the q–p formulation. Géotechnique 49 (5), 595–614.
Guo, X., Peng, C., Wu, W., Wang, Y., 2016. A hypoplastic constitutive model for debris materials. Acta Geotech. 11 (6), 1217–1229.
Guo, X., Peng, C., Wu, W., Wang, Y., 2021. Unified constitutive model for granular–fluid mixture in quasi-static and dense flow regimes. Acta Geotechnica 16 (3), 775–787.
Jefferies, M.G., 1993. Nor-Sand: a simle critical state model for sand. Géotechnique 43 (1), 91–103.
Jin, Y.F., Yin, Z.Y., Shen, S.L., Hicher, P.Y., 2016. Selection of sand models and identification of parameters using an enhanced genetic algorithm. Int. J. Numerical Anal. Methods Geomech. 40 (8), 1219–1240.
Jin, Y.F., Wu, Z.X., Yin, Z.Y., Shen, J.S., 2017. Estimation of critical state-related formula in advanced constitutive modeling of granular material. Acta Geotechnica 12, 1329–1351.
Jin, Y.F., Yin, Z.Y., Yuan, W.H., 2020. Simulating retrogressive slope failure using two different smoothed particle finite element methods: a comparative study. Eng. Geol. 279, 105870.
Jop, P., Forterre, Y., Pouliquen, O., 2006. A constitutive law for dense granular flows. Nature 441 (7094), 727–730.
Kamrin, K., 2010. Nonlinear elastoplastic model for dense granular flow. Int. J. Plasticity 26 (2), 167–188.
Lacaze, L., Kerswell, R.R., 2009. Axisymmetric granular collapse: a transient 3D flow test of viscoplasticity. Phys. Rev. Lett. 102 (10), 108305.
Landau, L.D., Lifshitz, E.M., 1987. Fluid Mechanics Butterworth.
Li, P., Shen, W., Hou, X., Li, T., 2019. Numerical simulation of the propagation process of a rapid flow-like landslide considering bed entrainment: a case study. Eng. Geol. 263, 105287.
Li, X.S., Dafalias, Y.F., Wang, Z.L., 1999. State-dependant dilatancy in critical-state constitutive modelling of sand. Can. Geotech. J. 36 (4), 599–611.
Liang, W., He, K.Y., Jin, Y.F., Yin, Z.Y., 2024. A gradient-smoothed material point method for reducing cell crossing noise in large deformation problems. Computers Geotechnics 169, 106169.
Liu, L.L., Zhang, P., Zhang, S.H., Li, J.Z., Huang, L., Cheng, Y.M., Wang, B., 2022. Efficient evaluation of run-out distance of slope failure under excavation. Eng. Geol. 306, 106751.
Lube, G., Huppert, H.E., Sparks, R.S.J., Hallworth, M.A., 2004. Axisymmetric collapses of granular columns. J. Fluid Mech. 508, 175–199.
Manzanal, D., Drempetic, V., Haddad, B., Pastor, M., Martin Stickle, M., Mira, P., 2016. Application of a new rheological model to rock avalanches: an SPH approach. Rock Mech. Rock. Eng. 49, 2353–2372.
Marveggio, P., Redaelli, I., Di Prisco, C., 2022. Phase transition in monodisperse granular materials: how to model it by using a strain hardening visco-elastic-plastic constitutive relationship. Int. J. Numer. Anal. Methods Geomech. 46 (13), 2415–2445.
Nova, R., Wood, D.M., 1982. A constitutive model for soil under monotonic and cyclic loading. Soil Mech. Transient Cyclic Load. 343–373.
Pastor, M., Blanc, T., Haddad, B., Drempetic, V., Morles, M.S., Dutto, P., Merodo, J.F., 2015a. Depth averaged models for fast landslide propagation: mathematical, rheological and numerical aspects. Arch. Comput. Methods Eng. 22, 67–104.
Pastor, M., Martin Stickle, M., Dutto, P., Mira, P., Fernández Merodo, J.A., Blanc, T., Sancho, S., Benítez, A.S., 2015b. A viscoplastic approach to the behaviour of fluidized geomaterials with application to fast landslides. Continuum Mech. Thermodyn. 27 (1–2), 21–47.
Pastor, M., Martin Stickle, M., Dutto, P., Mira, P., Fernández Merodo, J.A., Blanc, T., Benítez, A.S., 2015c. A viscoplastic approach to the behaviour of fluidized geomaterials with application to fast landslides. Contin. Mech. Thermodyn. 27, 21–47.
Peng, C., Guo, X., Wu, W., Wang, Y., 2016. Unified modelling of granular media with Smoothed Particle Hydrodynamics. Acta Geotechnica 11 (6), 1231–1247.
Perzyna, P., 1963. The constitutive equations for rate sensitive plastic materials. Q. Appl. Math. 20 (4), 321–332.
Ponthot, J.P., 2002. Unified stress update algorithms for the numerical simulation of large deformation elastoplastic and elasto-viscoplastic processes. Int. J. Plasticity 18 (1), 91–126.
Redaelli, I., Di Prisco, C., Vescovi, D., 2016. A visco-elasto-plastic model for granular materials under simple shear conditions. Int. J. Numerical Anal. Methods Geomech. 40 (1), 80–104.
Roscoe, K.H., Schofield, A., Wroth, A.P., 1958. On the yielding of soils. Geotechnique 8 (1), 22–53.
Savage, S.B., Sayed, M., 1984. Stresses developed by dry cohesionless granular materials sheared in an annular shear cell. J. Fluid Mech. 142, 391–430.
Schofield, A., Wroth, C., 1968. Critical State Soil Mechanics. McGraw-Hill, London, U.K.
Shen, W., Peng, J., Qiao, Z., Li, T., Li, P., Sun, X., Li, J., 2024. Plowing mechanism of rapid flow-like loess landslides: Insights from MPM modeling. Eng. Geol. 335, 107532.
Si, P., Shi, H., Yu, X., 2019. A general frictional-collisional model for dense granular flows. Landslides 16 (3), 485–496.
Sloan, S.W., Abbo, A.J., Sheng, D., 2001. Refined explicit integration of elastoplastic models with automatic error control. Eng. Comput. 18 (1/2), 121–194.
Su, B., Li, Y., Han, Z., Ma, Y., Wang, W., Ruan, B., Tan, S., 2024. Topography-based and vectorized algorithm for extracting physical quantities in 3D-SPH form and its application in debris-flow entrainment modeling. Eng. Geol. 340, 107693.
Urmi, Z.A., Yerro, A., Saeidi, A., Chavali, R.V.P., 2024. Prediction of retrogressive landslide in sensitive clays by incorporating a novel strain softening law into the Material Point Method. Eng. Geol. 340, 107669.
Vescovi, D., Di Prisco, C., Berzi, D., 2013. From solid to granular gases: the steady state for granular materials. Int. J. Numerical Anal. Methods Geomech. 37 (17), 2937–2951.
Vescovi, D., Redaelli, I., Di Prisco, C., 2020a. Modelling phase transition in granular materials: from discontinuum to continuum. Int. J. Solids Struct. 202, 495–510.
Vescovi, D., Marveggio, P., Di Prisco, C.G., 2020b. Saturated granular flows: constitutive modelling under steady simple shear conditions. Géotechnique 70 (7), 608–620.
Wang, Y., Wu, W., 2024. Hypoplastic model for solid-like and fluid-like granular flows. Comput. Geotech. 172, 106466.
Wichtmann, T., 2016. Soil Behaviour under Cyclic Loading—Experimental Observations, Constitutive Description and Applications. Habilitation, 181. Karlsruhe Institute for Technology, Institute of Soil Mechanics and Rock Mechanics.
Wu, W., Bauer, E., 1994. A simple hypoplastic constitutive model for sand. Int. J. Numerical Anal. Methods Geomech. 18 (12), 833–862.
Wu, W., Wang, S., Alipour, M., 2020. Constitutive Modelling for Fast Granular Flow.
Xu, T., Jin, Y.C., Tai, Y.C., Lu, C.H., 2017. Simulation of velocity and shear stress distributions in granular column collapses by a mesh-free method. J. Non-Newtonian Fluid Mech. 247, 146–164.
Xu, X., Jin, F., Sun, Q., Soga, K., Zhou, G.G.D., 2019. Three-dimensional material point method modeling of runout behavior of the Hongshiyan landslide. Can. Geotech. J. 56 (9), 1318–1337.
Yang, L., Zhang, M., Wang, L., Liu, T., Shi, P., Yin, B., Jiao, W., 2024. Failure kinematics and mechanisms of the 2019 Yahuokou flow-like landslide along the Pingding-Huama fault in Zhouqu segment. Eng. Geol. 332, 107448.
Yang, Y., Muraleetharan, K.K., 2003. The middle surface concept and its application to the elastoplastic behaviour of saturated sands. Geotechnique 53 (4), 421–431.
Yao, Y.-P., Hou, W., Zhou, A.-N., 2009. UH model: Three-dimensional unified hardening model for overconsolidated clays. Géotechnique 59 (5), 451–469.
Ye, T., Jiang, Q., Zhang, C., Ma, Z., Li, C., 2024. High-speed long-runout landslide scraping and entrainment effects: a case study on Shuicheng landslide. Eng. Geol. 341, 107722.
Yin, Z.Y., Jin, Z., Kotronis, Panagiotis, et al., 2018. Novel SPH simsand-based approach for modeling of granular collapse. Int. J. Geomech 18 (11), 04018156.
Yin, Z.-Y., Xu, Q., Hicher, P.-Y., 2013. A simple critical-state-based double-yield-surface model for clay behavior under complex loading. Acta Geotech. 8 (5), 509–523.
Yin, Z.-Y., Zhao, J., Hicher, P.-Y., 2014. A micromechanics-based model for sand-silt mixtures. Int. J. Solids Struct. 51 (6), 1350–1363.
Yin, Z.-Y., Hicher, P.-Y., Jin, Y.-F., 2020. Practice of Constitutive Modelling for Saturated Soils. Springer Singapore.